J. Fluid Mech. (1995), *vol.* 297, *pp.* 123–152

Finite deformation of liquid capsules enclosed by elastic membranes in simple shear flow

By C. POZRIKIDIS

Department of Applied Mechanics and Engineering Sciences, University of California at San Diego, La Jolla, CA 92093-0411, USA

(Received 7 December 1993 and in revised form 12 January 1995)

The transient deformation of liquid capsules enclosed by elastic membranes subject to simple shear flow is studied numerically using a new implementation of the boundary element method. The numerical results for capsules with spherical unstressed shapes and varying degrees of surface elasticity are compared with the predictions of an asymptotic theory for small deformations due to Barthès-Biesel and coworkers, and the significance of nonlinear effects due to finite deformation is assessed. It is found that the capsules exhibit continuous elongation when the dimensionless shear rate becomes larger than a critical threshold, in agreement with recent experimental observations of capsules with polymerized interfaces. Membrane failure at large deformations is discussed with respect to membrane thinning and development of excessive elastic tensions, and it is argued that the location where the membrane is likely to rupture due to continued deformation is insensitive to the precise mechanism of rupture. The numerical results suggest that a dilute suspension of capsules behaves like shear-thinning medium with some elastic properties. Results of oblate spheroidal capsules suggest that the points of maximum membrane thinning and tension coincide but their location depends upon the unstressed capsule shape.

1. Introduction

There has been growing interest in recent years in studying the behaviour of fluid particles with generalized interfacial properties, the simplest one being a liquid droplet with constant surface tension, and a more complex one being a red blood cell enclosed by a biological membrane. Such studies are motivated by the practical need to analyse the behaviour of droplets with contaminated interfaces, cells enclosed by biological membranes, and various synthetic capsules encountered in the chemical, biochemical, and allied industries, with applications in chemical and biomedical engineering.

The problem of flow past a liquid particle may be classified either as one of three-phase flow or as one of solid–fluid interaction. This is because the interface of the particle may be regarded either as a two dimensional Boussinesq medium whose rheological properties resemble those of a generalized two-dimensional fluid, or as a thin solid whose mechanical properties are analogous to those of a thin shell. In either case, the interfacial behaviour may be described under the auspices of continuum mechanics in terms of a set of physical constants including isotropic surface tension which is the analogue of the thermodynamic or hydrodynamic pressure, shear and dilatational viscosities, and modulii of elasticity.

Regarding an interface as a continuum is a phenomenological approach that overlooks the precise nature of intermolecular forces at the level of the microstructure and simplifies the three-dimensional nature of the interfacial layer. The uncertainties

in specifying the precise nature of interfacial transport mechanisms or measuring the values of the pertinent physical constants, however, justify the use of macroscopic models.

One example of a widely studied liquid capsule is the red blood cell. In this case the interface is a biological membrane that behaves like an incompressible viscoelastic solid at low shear rates, and like an incompressible two-dimensional fluid at high shear rates (Evans & Skalak 1980). In the second case, the isotropic component of the surface tension develops so that the surface area of the membrane remains locally and globally conserved, just as the pressure in an incompressible fluid develops so that the velocity field remains solenoidal at all times. Another common fluid capsule is a droplet of a monomeric solution with a polymerized interface whose mechanical behaviour has been described by a Kelvin–Voigt model (Chang & Olbright 1993).

In the present work we consider the deformation of liquid capsules whose interfaces exhibit purely elastic behaviour. Such capsules are regarded as acceptable models of red blood cells under conditions of small deformation, droplets with polymerized interfaces at low shear rates, and droplets whose interfaces are contaminated by organic substances. Furthermore, liquid capsules with thin-wall rubber membranes that behave like elastic shells have been used in the past as prototypes of red blood cells in experimental studies *in vitro* (Lee & Fung 1969; Sutera *et al.* 1970).

To place the present study into a more general framework of capsule dynamics, we briefly review previous work on capsule deformations in the presence of interfacial rheology. The starting point is Taylor's analysis of the small deformation of liquid drops with constant surface tension as formalized, refined, and extended by several subsequent authors (Stone 1994). The deformation of capsules bounded by elastic shells of finite or infinitesimal thickness have been considered on several occasions. Richardson (1974) computed the transient deformation of an oblate ellipsoidal capsule bounded by a linearly elastic shell subject to a simple shear flow during the initial period of the motion. Brunn (1980*a*, *b*) computed the flow around a slightly non-spherical capsule enclosed by an elastic shell of finite thickness subject to a general incident flow. Barthès-Biesel (1980) considered the steady shape of a nearly spherical capsule whose membrane tensions derive from the Mooney–Rivlin equation in simple shear flow, and Barthès-Biesel & Chhim (1981) studied the associated rheology of dilute suspensions. Extending this work in a two-fold way, Barthès-Biesel & Rallison (1981) considered the transient deformation subject to a general linear flow, and Barthès-Biesel & Sgaier (1985) incorporated the effects of surface viscosity. More recently, Li, Barthès-Biesel & Helmy (1988) computed large axisymmetric deformations of capsules with elastic interfaces subject to an axisymmetric stagnation-point flow for a variety of unstressed shapes, and Barthès-Biesel (1991) discussed the effect of interfacial properties on the behaviour of capsules in general linear shear flows.

The distinguishing features of the present study are that the initial unstressed capsule shape is allowed to be arbitrary, the membrane tension tensor derives from a general strain-energy function, and the motion is computed for finite deformations. The formulation of the problem relies heavily on the theoretical developments of Barthès-Biesel and coworkers (1980, 1981, 1985). The numerical results extend the asymptotic analyses for small deformation into the regime of finite deformations, thereby illustrating their range of validity, and address the effect of the unstressed capsule shape.

In the mathematical formulation we shall assume that the membrane is an infinitesimally thin elastic medium, and in the numerical computations we shall adopt a linearly elastic model for the interfacial behaviour pertinent to an incompressible

material. These are serious limitations that reduce the physical relevance of the model, especially with respect to membrane failure: a material with negative Poisson's ratio will thicken when it is stretched. It seems, however, that little can be done in the way of progress without such assumptions, at present, except for acknowledging these limitations.

The present computations are based on a new implementation of the boundary element method which is capable of handling general interfacial properties including viscoelasticity and incompressibility. Despite significant advances in the implementation of the method, high computational cost and the onset of numerical instabilities have forced us to restrict our attention to cases where the viscosity of the capsule is equal to that of the ambient liquid, the strain-energy function takes a simple form, the capsule deformation is finite but not excessively large, and the unstressed capsules are spherical or spheroidal with a moderate aspect ratio.

Recently, Chang & Olbright (1993) presented an experimental investigation of the deformation and breakup of capsules in simple shear flow. The capsules were fabricated using a novel technique that renders the interfaces polymerized layers with nearly spherical unstressed shapes. Assuming that the interfaces behave like a viscoelastic medium with a single modulus of elasticity that derives from the theory of small deformations, and comparing the observations with the predictions of the aforementioned asymptotic theory of Barthès-Biesel and coworkers, Chang & Olbright computed values of the effective interfacial modulus of elasticity and surface viscosity. Examining the present numerical results in the light of the observations of Chang & Olbright will allow us to discuss the significance of continued capsule deformations on membrane rupture in simple shear flow.

2. Mathematical formulation

We consider the transient deformation of a neutrally buoyant liquid capsule suspended in an unbounded ambient fluid with viscosity μ, subject to a simple shear flow along the x-axis with shear rate k, as shown in figure 1. The capsule contains a Newtonian fluid with viscosity $\lambda\mu$ and is bounded by a purely elastic interfacial layer of infinitesimal thickness and negligible mass. In the absence of the incident flow, the undeformed capsule may take an arbitrary unstressed shape in which the interfacial tensions vanish. The Reynolds number of the flow inside and around the capsule is assumed to be sufficiently small so that the motion of the fluid is governed by the equations of Stokes flow including the continuity equation and the Stokes equation.

In the mathematical model we regard the interface as a two-dimensional elastic medium. We then require that the velocity is continuous across the interface, but allow the hydrodynamic surface force or traction to undergo a discontinuity $\Delta \boldsymbol{f} = \boldsymbol{\sigma}^{(1)} \cdot \boldsymbol{n} - \boldsymbol{\sigma}^{(2)} \cdot \boldsymbol{n}$ that is balanced by the interfacial or membrane tensions, where $\boldsymbol{n}$ is the unit normal vector pointing into the ambient fluid. The boundary integral formulation for Stokes flow provides us with an integral equation for the velocity at the interface in terms of $\Delta \boldsymbol{f}$,

$$u_j(x_0) = \frac{2}{1+\lambda} u_j^{\infty}(x_0) - \frac{1}{4\pi\mu}\frac{1}{\lambda+1}\int_S \Delta f_i(x)\, G_{ij}(x, x_0)\, \mathrm{d}S(x)$$

$$+ \frac{\beta}{4\pi}\int_S^{PV} u_i(x)\, T_{ijk}(x, x_0)\, n_k(x)\, \mathrm{d}S(x), \quad (2.1)$$

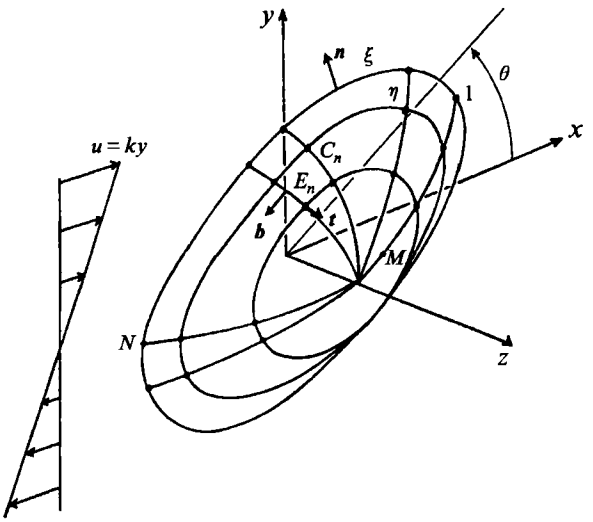

FIGURE 1. Schematic illustration of a capsule enclosed by an elastic membrane, deforming under the action of a simple shear flow along the x-axis. The shape of the membrane is described in terms of the curvilinear coordinates ξ and η.

where $\boldsymbol{u}^{\infty} = (ky, 0, 0)$ is the incident shear flow, the point $\boldsymbol{x}_0$ is located on the interface which is denoted by S, $\beta = (\lambda - 1)/(\lambda + 1)$, and

$$G_{ij}(\boldsymbol{x}, \boldsymbol{x}_0) = \frac{\delta_{ij}}{|\hat{\boldsymbol{x}}|} + \frac{\hat{x}_i \hat{x}_j}{|\hat{\boldsymbol{x}}|^3}, \quad T_{ijk}(\boldsymbol{x}, \boldsymbol{x}_0) = -6\frac{\hat{x}_i \hat{x}_j \hat{x}_k}{|\hat{\boldsymbol{x}}|^5}, \quad \text{with} \quad \hat{\boldsymbol{x}} = \boldsymbol{x} - \boldsymbol{x}_0 \tag{2.2}$$

are respectively the free-space Green function for the velocity and stress (Pozrikidis 1992, Chap. 5). The first and second integrals on the right-hand side of (2.1) are, respectively, the single-layer and double-layer hydrodynamic potentials for Stokes flow, and PV denotes the principal value of the improper double-layer integral. Given $\Delta \boldsymbol{f}$, we solve (2.1) for the interfacial velocity and advance the position of material point particles over the interface, thus describing the deformation of the capsule.

The direction and magnitude of the traction discontinuity $\Delta \boldsymbol{f}$ depends upon the developing elastic tensions. Neglecting interfacial bending moments allows us to assume that the tensions act in the plane of the interface and may thus be described by the two-dimensional elastic tension tensor $\boldsymbol{T}$. A force balance over a section of the membrane D that is enclosed by the contour C yields

$$\int_D \Delta \boldsymbol{f} \, \mathrm{d}S = -\int_C \boldsymbol{T} \cdot (\boldsymbol{t} \times \boldsymbol{n}) \, \mathrm{d}l, \tag{2.3}$$

where $\boldsymbol{t}$ is the unit vector tangential to C directed in the counterclockwise sense with respect to $\boldsymbol{n}$. The unit vector $\boldsymbol{t} \times \boldsymbol{n}$ is tangential to the interface and normal to the contour C. Taking the limit as D vanishes and using the divergence theorem we recast (2.3) to the differential form

$$\Delta \boldsymbol{f} = (\boldsymbol{I} - \boldsymbol{nn}) \cdot \nabla \cdot \boldsymbol{T}. \tag{2.4}$$

The right-hand side of (2.4) is the surface divergence of $\boldsymbol{T}$. This completes the definition of the hydrodynamic problem. Our next task will be to relate $\boldsymbol{T}$ to the interfacial deformations.

2.1. *Elastic tensions*

To compute the instantaneous elastic tensions we relate them to the Green or material strain tensor using a constitutive equation that involves the surface strain-energy function (Novozhilov 1962). Skalak *et al.* (1973) developed the constitutive equation in global Cartesian co-ordinates in terms of the surface Piola–Kirchoff tensor, whereas Barthès-Biesel (1980) developed an alternative formulation in surface curvilinear coordinates. Subsequently, Barthès-Biesel & Rallison (1981) noted that the coupling of the fluid stresses on either side of the interface and the interfacial tensions is done most effectively in Cartesian coordinates, and rederived the constitutive equation in a form that is readily accessible to analytical and numerical computation. An analogous development for interfaces with viscous behaviour was presented almost simultaneously by Secomb & Skalak (1982). The main steps in the formulation of Barthès-Biesel & Rallison (1981) will now be briefly outlined using the evolved notation of Barthès-Biesel & Sgaier (1985) and with reference to the original formalism of Skalak *et al.* (1973).

Let us denote the Cartesian coordinates of a point particle on the interface at the initial instant when the interface is unstressed by $\boldsymbol{X}$, and at some later time t by $\boldsymbol{x}$. We extend the interface into the three-dimensional space, and assume that there are no deformations of the extended solid material in planes that are normal to the interface; effectively this implies that planes that are normal to the interface remain normal to the interface at all times. Assuming that a material vector that is initially normal to the interface remains normal to the interface at all times, we extend the domains of definition of $\boldsymbol{X}$ and $\boldsymbol{x}$ off the interface, and introduce the three-dimensional relative deformation gradient $\boldsymbol{F}$ defined over the interface by

$$\mathrm{d}\boldsymbol{x} = \boldsymbol{F}(\boldsymbol{X}, t)\cdot \mathrm{d}\boldsymbol{X}. \tag{2.5}$$

Next, we introduce the interfacial relative deformation gradient $\boldsymbol{A} = \boldsymbol{F}\cdot(\boldsymbol{I}-\boldsymbol{NN})$ where $\boldsymbol{N}$ is the unit vector normal to the interface at the initial instant corresponding to the unstressed shape. The distinguishing feature of $\boldsymbol{A}$ is that $\boldsymbol{A}\cdot \mathrm{d}\boldsymbol{X} = \boldsymbol{F}\cdot \mathrm{d}\boldsymbol{X}$ when $\mathrm{d}\boldsymbol{X}$ is in the plane of the interface, and $\boldsymbol{A}\cdot \mathrm{d}\boldsymbol{X} = 0$ when $\mathrm{d}\boldsymbol{X}$ is normal to the interface, which implies that $\boldsymbol{A}\cdot\boldsymbol{N} = 0$. The last equation reveals that $\boldsymbol{N}$ is an eigenvector of $\boldsymbol{A}$ with corresponding eigenvalue equal to zero, which means that $\boldsymbol{A}$ is singular. After the interface has been deformed, two orthonormal material vectors $\boldsymbol{T}_1$ and $\boldsymbol{T}_2$ that are tangential to the undeformed interface at a point will become $\boldsymbol{t}_1$ and $\boldsymbol{t}_2$, where the last two vectors are not necessarily unit vectors. Writing $\boldsymbol{I}-\boldsymbol{NN} = \boldsymbol{T}_1\boldsymbol{T}_1+\boldsymbol{T}_2\boldsymbol{T}_2$ we compute $\boldsymbol{n}\cdot\boldsymbol{A} = \boldsymbol{n}\cdot\boldsymbol{F}\cdot(\boldsymbol{T}_1\boldsymbol{T}_1+\boldsymbol{T}_2\boldsymbol{T}_2) = \boldsymbol{n}\cdot(\boldsymbol{t}_1\boldsymbol{T}_1+\boldsymbol{t}_2\boldsymbol{T}_2) = 0$ which implies that $\boldsymbol{A} = (\boldsymbol{I}-\boldsymbol{nn})\cdot\boldsymbol{A}$ or

$$\boldsymbol{A} = (\boldsymbol{I}-\boldsymbol{nn})\cdot\boldsymbol{F}\cdot(\boldsymbol{I}-\boldsymbol{NN}). \tag{2.6}$$

Following standard procedure, we introduce the symmetric surface Cauchy–Green strain tensor

$$\boldsymbol{\Lambda}^2 = \boldsymbol{A}\cdot\boldsymbol{A}^T, \tag{2.7}$$

where the superscript T designates the transpose. The eigenvalues of $\boldsymbol{\Lambda}^2$ are equal to λ_1^2, λ_2^2 and 0, where λ_1 and λ_2 are the principal extension ratios in the plane of the interface. The corresponding eigenvectors are composed of two mutually orthogonal tangential vectors and the normal vector $\boldsymbol{n}$. The local area stretch of the interface is equal to $\lambda_1\lambda_2$. Skalak *et al.* (1973) introduced the strain invariants

$$I_1 = \lambda_1^2+\lambda_2^2-2 = \mathrm{trace}\,(\boldsymbol{\Lambda}^2)-2, \quad I_2 = (\lambda_1\lambda_2)^2-1. \tag{2.8}$$

The purpose of introducing I_2 in this particular form is to have an invariant that vanishes when the area of the interface is locally conserved, which is useful in modelling the membrane of a red blood cell. Barthès-Biesel & Rallison (1981) introduced the alternative invariants

$$\left.\begin{aligned} \Lambda_1 = \ln(\lambda_1\lambda_2) = \tfrac{1}{2}\ln\{\tfrac{1}{2}[\mathrm{trace}^2(\mathbf{\Lambda}^2) - \mathrm{trace}(\mathbf{\Lambda}^4)]\} = \tfrac{1}{2}\ln(I_2+1), \\ \Lambda_2 = \tfrac{1}{2}I_1 \end{aligned}\right\} \tag{2.9}$$

which are appropriate for more general elastic behaviours. Both I_2 and Λ_1 vanish when the local areal stretch is equal to one, in which case all interfacial patches maintain their original surface area.

Barthès-Biesel & Rallison (1981) showed that the interfacial stress tensor derives from a surface strain energy function $W(\Lambda_1, \Lambda_2)$ by means of the equation

$$\boldsymbol{T} = \frac{1}{\lambda_1\lambda_2}\left[\frac{\partial W}{\partial \Lambda_1}(\boldsymbol{I}-\boldsymbol{nn}) + \frac{\partial W}{\partial \Lambda_2}\mathbf{\Lambda}^2\right]. \tag{2.10}$$

In the unstressed state $\mathbf{\Lambda}^2 = \boldsymbol{I}-\boldsymbol{nn}$ and we must have $\partial W/\partial\Lambda_1 + \partial W/\partial\Lambda_2 = 0$ in order for $\boldsymbol{T} = 0$. When the deformations are small, the strain-energy function may be expanded in a Taylor series with respect to Λ_1 and Λ_2 which may be placed in the standard form

$$W = \alpha_0 + (\alpha_1-\alpha_3)\Lambda_1 + \alpha_3\Lambda_2 + \tfrac{1}{2}(\alpha_1+\alpha_2)\Lambda_1^2 + \ldots, \tag{2.11}$$

where α_i are material constants, and α_0 may be assigned an arbitrary value with no consequences on the magnitude of the interfacial tensions.

Considering the asymptotic behaviour of a three-dimensional elastic shell which in the unstressed state has a small uniform thickness h, we find that, in the limit as h vanishes,

$$\alpha_1 = 0, \quad \alpha_2 = \tfrac{2}{3}Eh, \quad \alpha_3 = \tfrac{1}{3}Eh, \tag{2.12}$$

where E is the bulk Young modulus of elasticity of the three-dimensional material (Barthès-Biesel & Rallison 1981). In this case (2.10) takes the simplified form

$$\boldsymbol{T} = \frac{Eh}{3\lambda_1\lambda_2}\{(2\Lambda_1-1)[\boldsymbol{I}-\boldsymbol{nn}] + \mathbf{\Lambda}^2\}. \tag{2.13}$$

In the unstressed state $\Lambda_1 = 0$ and $\mathbf{\Lambda}^2 = \boldsymbol{I}-\boldsymbol{nn}$ which implies that $\boldsymbol{T} = 0$.

Skalak *et al.* (1973) proposed modelling the membrane of a red blood cell in terms of the strain-energy function

$$W = \tfrac{1}{4}B(\tfrac{1}{2}I_1^2 + I_1 - I_2) + \tfrac{1}{8}CI_2^2 = \tfrac{1}{4}B[2\Lambda_2(\Lambda_2+1) + 1 - \mathrm{e}^{2\Lambda_1}] + \tfrac{1}{8}C(\mathrm{e}^{2\Lambda_1}-1)^2, \tag{2.14}$$

where B and C are material property constants whose values are deduced from experimental observations.

2.2. *Particle stress tensor*

The shape of the capsule and the instantaneous interfacial velocity field may be used to compute the effective stress tensor $\langle\boldsymbol{\sigma}\rangle$ of a dilute emulsion of drops in simple shear flow. Following Batchelor (1970) and Pozrikidis (1993) we find

$$\langle\sigma_{ij}\rangle = -\delta_{ij}\langle P\rangle + 2\mu_1\langle e_{ij}\rangle + \Phi\int_{Capsule}[\Delta f_i x_j - \mu(1-\lambda)(u_i n_j + u_j n_i)]\,\mathrm{d}S, \tag{2.15}$$

where $\langle\ \rangle$ signifies volume average values and Φ is the number of drops per unit volume of the suspension. The integral on the right-hand side of (2.15) is known as the *stresslet* or *particle stress tensor*, and will be denoted by $\boldsymbol{\Sigma}$.

3. Numerical method

To describe the motion of the interface we introduce two surface coordinates ξ and η, construct a curvilinear surface grid of size N by M as shown in figure 1, and then compute the motion of marker points that lie at the intersections of grid lines. At the initial instant, the ξ-lines are lines of constant z, evenly distributed with respect to the azimuthal angle, and the η-lines are lines of constant meridional angle θ. The marker points are Lagrangian point particles, and as such they move with the velocity of the fluid. The intersections between two successive surface coordinate lines defines a set quadrilateral boundary elements over the main body of the cell and a set of triangular elements with a node on the z-axis.

To compute the traction discontinuity $\Delta \boldsymbol{f}$ from equation (2.4) we require the surface divergence of the interfacial tension, but the computation of the latter involves high-order differentiations that worsen the accuracy of the numerical method. To circumvent this difficulty, we replace the single-layer integral on the right-hand side of (2.1) with a sum of integrals over all boundary elements E_n, and implement a special version of the trapezoidal rule, writing

$$\frac{1}{S_n}\int_{E_n} \Delta f_i(\boldsymbol{x})\, G_{ij}(\boldsymbol{x}, \boldsymbol{x}_0)\, \mathrm{d}S(\boldsymbol{x}) \approx \langle \Delta f_i \rangle_n \langle \Delta G_{ij} \rangle_n, \tag{3.1}$$

$$\text{where} \quad \langle \Delta f_i \rangle_n \equiv \frac{1}{S_n}\int_{E_n} \Delta f_i(\boldsymbol{x})\, \mathrm{d}S(\boldsymbol{x}), \quad \langle G_{ij} \rangle_n (\boldsymbol{x}_0) \equiv \frac{1}{S_n}\int_{E_n} G_{ij}(\boldsymbol{x}, \boldsymbol{x}_0)\, \mathrm{d}S(\boldsymbol{x}) \tag{3.2}$$

are the mean values of the discontinuity in the interfacial surface force and Green's function over the nth element, and S_n is the surface area of the nth element. Approximations similar to the one shown in (3.1) were used previously by the present author to compute the deformation of drops with constant surface tension and viscous interfacial behaviour, as well as the deformation of capsules with the incompressible interfaces characterized by isotropic tension (Pozrikidis 1993, 1994; Zhou & Pozrikidis 1995). Using the force balance in equation (2.3) we obtain

$$\langle \Delta f_i \rangle_n = -\frac{1}{S_n}\int_{C_n} T_{ij}(\boldsymbol{x})\, b_k(\boldsymbol{x})\, \mathrm{d}l(\boldsymbol{x}), \tag{3.3}$$

where C_n is the contour of the element E_n, $\boldsymbol{b} = \boldsymbol{t} \times \boldsymbol{n}$, and $\boldsymbol{t}$ is the unit vector tangential to C_n pointing in the counterclockwise with respect to the normal vector as shown in figure 1. The contour integral in (3.3) is computed using the one-step trapezoidal rule, which requires knowledge of the value of the elastic tensions at the surface grid points. The latter are computed in a straightforward manner using (2.10) where all necessary differentiations are carried out using central differences with respect to the curvilinear surface cordinates.

The three-dimensional relative deformation gradient $\boldsymbol{F}$ is computed by solving three systems of linear equations for the three rows of $\boldsymbol{F}$ that derive by applying (2.5) for the two material tangential vectors $\partial \boldsymbol{X}/\partial\xi$ and $\partial \boldsymbol{X}/\partial\eta$ and the normal vector $\boldsymbol{N}$ at the grid points, yielding $\partial \boldsymbol{x}/\partial\xi = \boldsymbol{F}\cdot\partial \boldsymbol{X}/\partial\xi$, $\partial \boldsymbol{x}/\partial\eta = \boldsymbol{F}\cdot\partial \boldsymbol{X}/\partial\eta$, and $\beta \boldsymbol{n} = \boldsymbol{F}\cdot\boldsymbol{N}$, where β is an arbitrary scalar coefficient. Having obtained $\boldsymbol{F}$, we compute $\boldsymbol{A}$ using equation (2.6). Equivalently, we may obtain the three rows of $\boldsymbol{A}$ directly by solving three systems of linear equations that derive from $\partial \boldsymbol{x}/\partial\xi = \boldsymbol{A}\cdot\partial \boldsymbol{X}/\partial\xi$, $\partial \boldsymbol{x}/\partial\eta = \boldsymbol{A}\cdot\partial \boldsymbol{X}/\partial\eta$, and $0 = \boldsymbol{F}\cdot\boldsymbol{N}$. Having obtained $\boldsymbol{A}$, we compute $\boldsymbol{\Lambda}^2$ using equation (2.7), and then recover the tensions

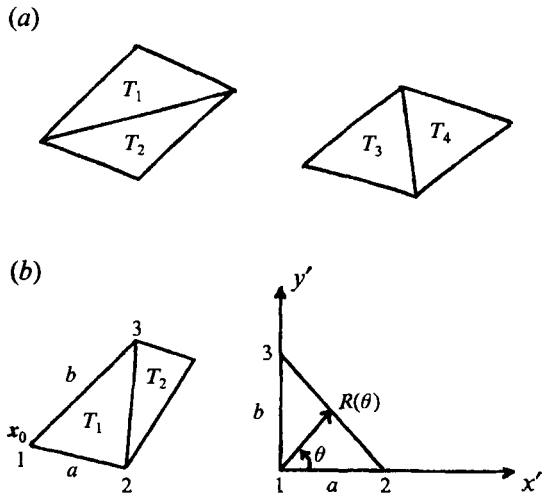

FIGURE 2. (*a*) To compute the single-layer integral, each quadrilateral boundary element is subdivided into four flat triangles, and the non-singular integrals over the triangles are computed using a quadrature. (*b*) When the point x_0 is located at a vertex of an element, the single-layer integral becomes singular. In this case the element is divided into a non-singular and a singular triangle, and the singular integral is computed by mapping the singular triangle into the (x', y')-plane and performing the integration in plane polar coordinates.

from (2.10). The tension tensor at the singular grid point that lies on the z-axis is computed by quadratic extrapolation using the mean values of the tension at the two previous η grid lines.

The single-layer integral on the right-hand side of (3.1) over the nth quadrilateral element evaluated at a point x_0 that is located off the element, is computed according to the formula

$$\langle G_{ij}\rangle_n(x_0) = \frac{1}{2}\left[\frac{1}{S_{n,1}+S_{n,2}}\sum_{k=1}^{2}\int_{T_{n,k}} G_{ij}(x,x_0)\,dS(x) + \frac{1}{S_{n,3}+S_{n,4}}\sum_{k=3}^{4}\int_{T_{n,k}} G_{ij}(x,x_0)\,dS(x)\right], \quad (3.4)$$

where $T_{n,k}$, $k = 1,2,3,4$, designates the four planar triangles that may be formed by connecting the vertices of the nth element as shown in figure 2(*a*), and $S_{n,k}$ are the corresponding surface areas. This particular formulation prevents the geometrical bias due to the preferential element triangulation into one of the two pairs (T_1, T_2) or (T_3, T_4). The integrals over the triangles are computed using the three-point Gaussian quadrature for a triangular domain, which approximates the integral by the product of the area of the triangle and the mean value of the Green function evaluated at the mid-points of each one of the three sides.

The single-layer integral is singular when the point x_0 is located at one of the vertices of a quadrilateral element as shown in figure 2(*b*). In this case we discretize the element into two triangles, only one of which contains the singular point as shown in figure 2(*b*), and write

$$\langle G_{ij}\rangle_n(x_0) = \frac{1}{S_{n,1}+S_{n,2}}\sum_{k=1}^{2}\int_{T_{n,k}} G_{ij}(x,x_0)\,dS(x). \quad (3.5)$$

The integral over the non-singular triangle $T_{n,2}$ is computed using the three- or four-point Gaussian quadrature as mentioned above. To compute the singular integral over the triangle $T_{n,1}$ we map it onto a right-angled triangle in the (x', y')-plane shown in figure 2(*b*), using the linear mapping function

$$x = x_1 + \frac{x'}{a}(x_2 - x_1) + \frac{y'}{b}(x_3 - x_1), \tag{3.6}$$

where $a = |x_2 - x_1|$ and $b = |x_3 - x_1|$, and remove the singularity by working in local polar coordinates according to the formula

$$\frac{1}{S_{n,1}} \int_{T_{n,1}} G_{ij}(x, x_0)\, \mathrm{d}S(x) = \frac{\displaystyle\int_0^{\pi/2} \int_0^{R(\theta)} G_{ij}(x, x_0)\, \rho\, \mathrm{d}\rho\, \mathrm{d}\theta}{\displaystyle\int_0^{\pi/2} \int_0^{R(\theta)} \rho\, \mathrm{d}\rho\, \mathrm{d}\theta}, \tag{3.7}$$

where $R(\theta) = ab/(a\sin\theta + b\cos\theta)$. The two integrals on the right-hand side of (3.7) over ρ and θ are computed using the four- or six-point Gauss–Legendre quadrature for integration in each direction.

Large computational cost made it necessary to restrict our attention to the case $\lambda = 1$ for which the coefficient of the double-layer integral on the right-hand side of (2.1) vanishes. Preliminary computations using a crude method for evaluating the double-layer integral showed that the iterative solution of the integral equation for other values of λ requires a prohibitive computational cost. For instance, for $\lambda = 5$ and with a $N = 16$ by $M = 8$ grid, the solution of the integral equation requires about 15 mins of CPU time on the workstation described below.

After the velocity at the grid points has been computed, the position of the marker points is advanced with the velocity of the fluid using Euler's method. The performance of the numerical method depends upon the magnitude of the elastic tensions and the degree of capsule deformation. Sawtooth instabilities arise, but may be effectively controlled by reducing the size of the time step Δt to a sufficiently small level. The origin of these instabilities is probably similar to that for liquid drops with isotropic surface tension (Kennedy, Pozrikidis & Skalak 1994). Note that similar difficulties have been reported for the analogous problem of flow in the heart where the action of the muscle is modelled in terms of elastic link structures (Peskin & McQueen 1980). Furthermore, an increasingly small time step is required at the late stages of the motion when the capsules deforms and reaches a nearly stationary shape, and when a capsule deforms and is then allowed to relax back to the initial unstressed shape.

One effective way of filtering out the instabilities is to apply numerical smoothing according to which the marker points along the ξ-lines are repositioned using the five-point smoothing formula of Longuet-Higgins & Cokelet (1976) after the completion of each time step. The effect of smoothing on the accuracy of the results will be discussed in the next section. The maximum value of Δt for a stable computation depends upon the size of the interfacial grid and the values of the surface elasticity: as the grid becomes finer and the surface elasticity is increased, a smaller Δt is required. For the $N = 16$, $M = 8$ grid used in the majority of the computations, $k\Delta t$ ranged between 0.01 and 0.001 across the parametric studies, with an average of 200 time steps for a complete computation.

The majority of the computations were performed with a standard $N = 16$ and $M = 8$ grid, but some experimentation was done with a finer grid as will be discussed in §4. The volume of a capsule changed by less than 1% of the initial value from the

beginning to the end of a computation. All computations were performed on a SUN SPACstation IPC with 24 Mb of RAM. For the simple case $\lambda = 1$, one velocity evaluation requires approximately 2 min of CPU time.

4. Spherical capsules

In the present section we consider the deformation of capsules with spherical unstressed shapes bounded by elastic membranes whose strain-energy function is described by (2.11) and (2.12) with the membrane tension given by (2.13). Strictly speaking, these equations apply only in the limit of small deformations, but in order to reduce the parametric space of our investigation and establish a point of reference, we shall assume that they remain valid even when the deformations are not small.

Non-dimensionalizing all lengths by the undeformed capsule radius a, time by the inverse shear rate $1/k$, velocity by ak, stresses by μk, and tensions by μka, we find that the behaviour of the capsule depends upon the viscosity ratio λ and the dimensionless shear rate $G = \mu ka/Eh$ where E is the Young modulus of elasticity and h is the membrane thickness in the unstressed state. It is worth noting that G is analogous to the capillary number $Ca = \mu ka/\gamma$ applicable for drops with constant interfacial tension γ. For the reasons stated in the preceding section, we shall confine our attention to the case $\lambda = 1$ and examine the motion as a function of the dimensionless shear rate G alone.

4.1. *Small-deformation theory*

Barthès-Biesel & Rallison (1981) studied the transient deformation of spherical capsules in a general linear flow, under the assumption that the deformation is sufficiently small so that all variables may be expanded in an asymptotic series with respect to a properly defined small-deformation parameter. Maintaining first-order terms in the expansions, they found that when the capsule is immersed in a simple shear flow, the position of material points over the interface is given by

$$\boldsymbol{x}(t) = \boldsymbol{x}'(t) + K(t)[y', x', 0] + 2I(t)\frac{x'y'}{a|\boldsymbol{x}'|}[x', y', 0], \tag{4.1}$$

where

$$\frac{\mathrm{d}\boldsymbol{x}'(t)}{\mathrm{d}t} = k\frac{1}{2}\begin{bmatrix} 0 & 1 & 0 \\ -1 & 0 & 0 \\ 0 & 0 & 0 \end{bmatrix} \cdot \boldsymbol{x}'(t). \tag{4.2}$$

Physically, $\boldsymbol{x}'$ would be the location of point particles if the undeformed spherical capsule rotated like a rigid body with angular velocity equal to half the vorticity of the incident shear flow; $\boldsymbol{x}'(0) = \boldsymbol{X}$ is the position of the point particles at the initial instant. The dimensionless functions K and I evolve according to the linear equations

$$\frac{\mathrm{d}K}{\mathrm{d}t} = \frac{5}{2\lambda+3}\left(\frac{1}{2} + \frac{1}{5}L + \frac{2}{5}\frac{3\lambda+2}{19\lambda+16}M\right), \quad \frac{\mathrm{d}I}{\mathrm{d}t} = \frac{2}{19\lambda+16}M, \tag{4.3}$$

where the auxiliary dimensionless functions L and M are defined as

$$\left.\begin{aligned} L &= \frac{1}{\mu ka}[4(\alpha_2+\alpha_3)J - (6\alpha_2+10\alpha_3)K], \\ M &= \frac{1}{\mu ka}[-4(\alpha_1+2\alpha_2+2\alpha_3)J + (12\alpha_2+16\alpha_3)K], \end{aligned}\right\} \tag{4.4}$$

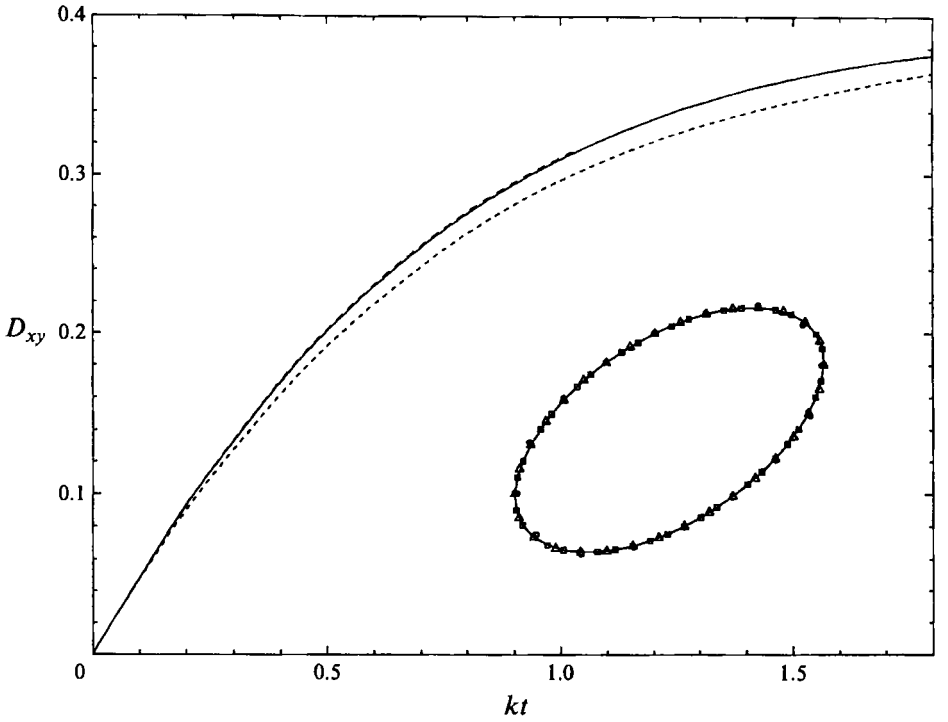

FIGURE 3. Convergence of the numerical results with respect to the grid size for the evolution of the deformation parameter D_{xy} for an initially spherical capsule at dimensionless shear rate $G = 0.10$. The short-dashed, solid, and long-dashed lines represent, respectively, results with grids of size (N, M) equal to (8, 4), (16, 8), and (24, 12). The inset shows the location of the marker points in the (x, y)-plane at time $kt = 1.03$ with triangles, circles, and squares for the coarse, intermediate, and fine grid.

with $J = I + K$. The coefficients α_i are identical to the material constants that appear in the expansion (2.11).

4.2. *Numerical accuracy*

Before discussing the numerical results we address the accuracy of the computations by plotting the evolution of the deformation parameter $D_{xy} = (L-B)/(L+B)$, where L and B are the maximum and minimum radial distances of the contour of the capsule in the (x, y)-plane from the origin, for $G = 0.10$, computed using a progressively finer grid with (N, M) equal to (8, 4), (16, 8), and (24, 12) (figure 3). The long-dashed line, corresponding to the finest grid, lies close the solid line, corresponding to the intermediate grid, and this suggests that the intermediate grid yields satisfactory accuracy for moderate and large deformations. Consequently, the (16, 8) grid was adopted as the standard grid in the main body of the parametric investigation.

To further demonstrate the effect of the grid size, in the inset of figure 3 we plot the instantaneous position of the marker points in the (x, y)-plane at $kt = 1.03$ for the three grids mentioned above, and connect the marker points to obtain visually indistinguishable contours. It is surprising that even the crude (8, 4) grid is able to describe the shape of the capsule with sufficient accuracy. The accuracy of the numerical results will be further confirmed by comparing the numerical results with the predictions of the small-deformation theory.

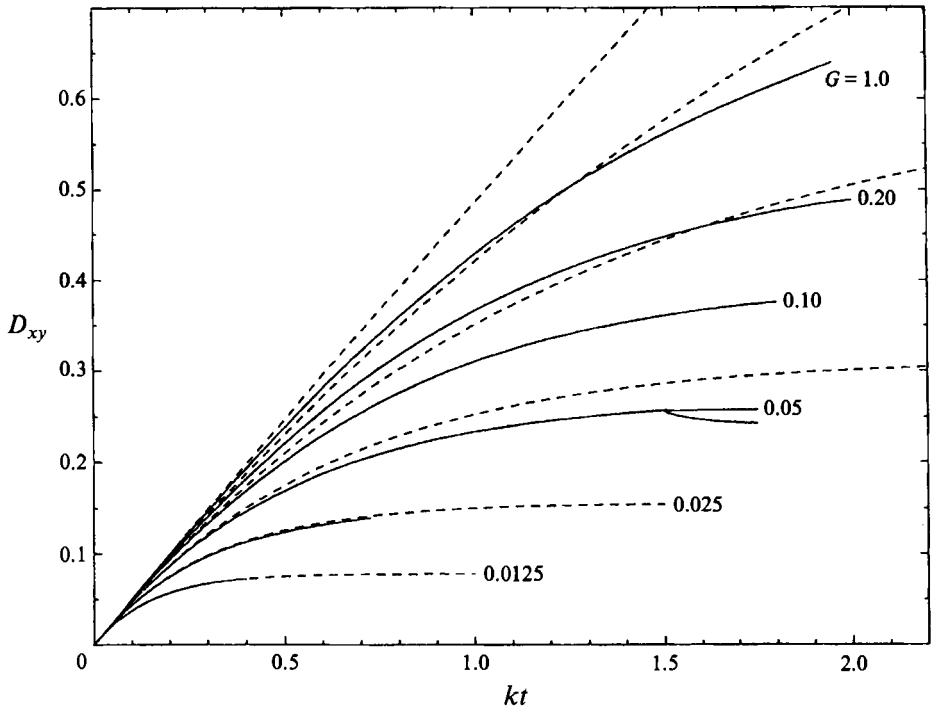

FIGURE 4. The evolution of the deformation parameter D_{xy} at a sequence of dimensionless shear rates G. The dashed lines represent the predictions of the first-order linear theory for small deformations. The line branching off the tail-end of the curve for $G = 0.05$ corresponds to a computation with numerical smoothing.

4.3. *Transient and asymptotic deformations*

In figure 4 we plot the evolution of the Taylor deformation parameter D_{xy} defined previously for a sequence of dimensionless shear rates. The numerical results are represented by the solid lines, and the predictions of the linearized system (4.1) are represented by the dashed lines. The latter predicts that, at long times, D_{xy} tends to a steady value that is equal to $D_{xy}^{\infty} = (25/4)G$. When $G = 0.0125$ and 0.025, in which cases the deformations are small and moderate throughout the evolution, the numerical results are in excellent agreement with the predictions of the small-deformation theory. At long times, the capsule assumes a stationary shape whose estimated asymptotic deformation, $D_{xy}^{\infty} = 0.078$ and 0.156, is predicted with high accuracy by the linear model. When $G = 0.05$ the agreement between the numerical results and the asymptotic predictions is good during the initial period of deformation, but deteriorates at later times. The asymptotic deformation $D_{xy}^{\infty} = 0.27$ emerging from the numerical computations is substantially lower than that predicted by the small-deformation theory which is equal to 0.313. Similar discrepancies between the numerical results and the predictions of the linear theory at finite deformations are observed for $G = 0.10$, 0.20. The extrapolated asymptotic deformations at long times, $D_{xy}^{\infty} = 0.40$ and 0.53, are significantly lower than those predicted by the linear model.

As mentioned in §3, as the capsules approach a steady state, a progressively smaller time step must be used in order to suppress the sawtooth-type numerical instabilities, but this occurrence leads to prohibitively long computational times. A compromise would be to apply numerical smoothing as discussed in §3. The small curve branching

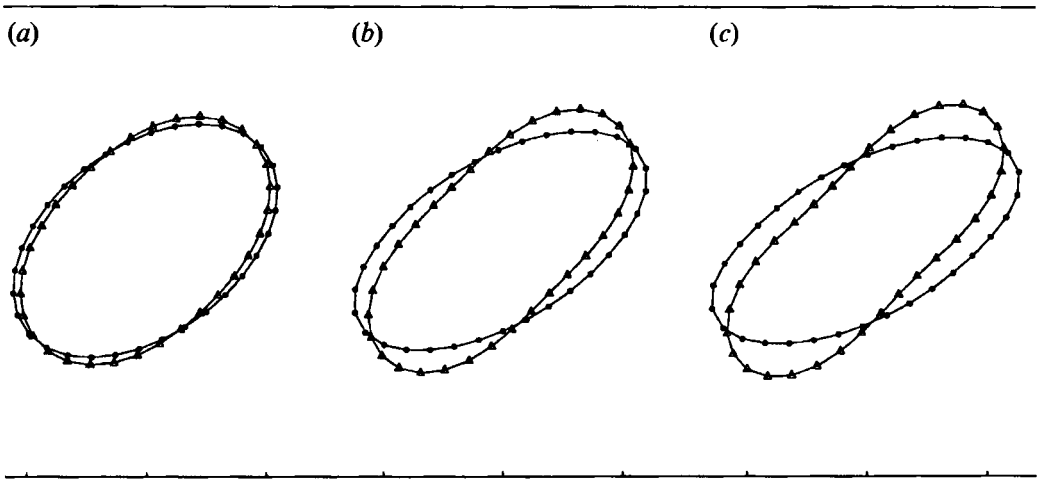

FIGURE 5. The location of marker points in the (x, y)-plane as computed by the present numerical method (circles) and predicted by the first-order small-deformation theory (triangles) for $G = 0.10$, at times (*a*) $kt = 0.60$, (*b*) $kt = 1.23$, (*c*) $kt = 1.80$.

off the tail end of the deformation curve for $G = 0.05$ in figure 4 corresponds to a computation with smoothing, but the asymptotic deformation predicted using this modification is substantially lower than that corresponding to the computation without smoothing. The effect of smoothing on the shape of the capsule becomes milder as the grid size becomes finer.

To examine the physical origin of the differences between the predictions of the linear theory and the results of the numerical computations at finite deformations, we compare the predicted and computed capsule shapes at different stages of the motion. In figure 5(*a–c*) we plot with circles the computed location of the grid points in the (x, y)-plane for $G = 0.10$, and with triangles the corresponding predictions of the linear model, at three time instants. At small deformations the agreement is acceptable, but at moderate and large deformations we observe significant deviations. The linear theory, in particular, predicts that the capsule deforms along the principal direction of the rate of strain of the shear flow, which forms a 45° angle with respect to the x-axis, whereas the numerical results show that the inclination is reduced during the deformation.

Returning to figure 4 we note that when the dimensionless shear rate G is set to unity, the capsule continues to deform without showing evidence that it reaches a steady shape, and the computations are interrupted when the grid fails to resolve the fine structure of the interface with adequate resolution. Whether continued deformation will lead to breakup or the capsule will assume a highly distorted steady shape cannot be stated with confidence. Continued deformation occurs when D_{xy} exceeds roughly the value of 0.55, and the critical value of G above which the capsule fails to reach a stationary shape is estimated to be close to but above the value of 0.20. For comparison, we note that the critical value of the capillary number above which drops with $\lambda = 1$ and constant surface tension γ exhibit continued elongation is $Ca = 0.37$ (Kennedy *et al.* 1994).

In figure 6 we plot the computed asymptotic capsule deformation D_{xy}^{∞} as a function of G and obtain a concave curve that terminates at about $G = 0.20$. The shape of this curve is similar to that for viscous drops with constant surface tension at values of the viscosity ratio λ larger than 4 (Kennedy *et al.* 1994). At small deformations the

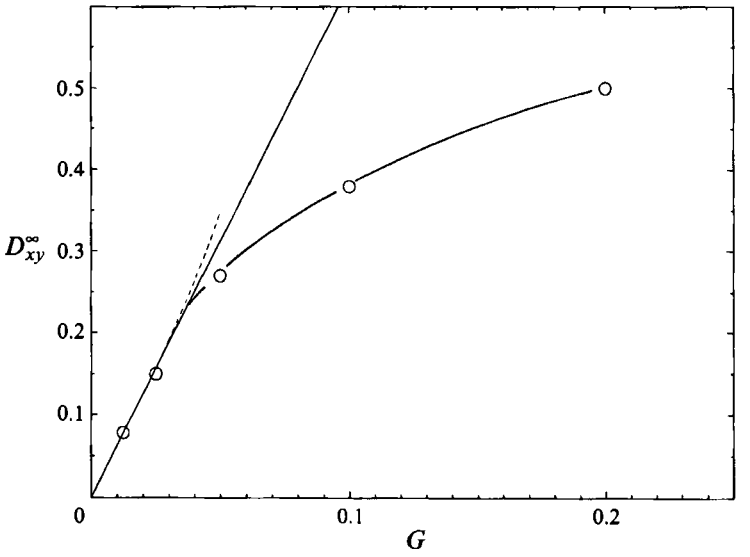

FIGURE 6. The extrapolated asymptotic deformation at long times D^{∞}_{xy} as a function of the dimensionless shear rate G. The curve terminates at a critical shear rate that is close to 0.20. The solid and dashed lines show, respectively, the predictions of the first- and second-order theory of Barthès-Biesel (1980).

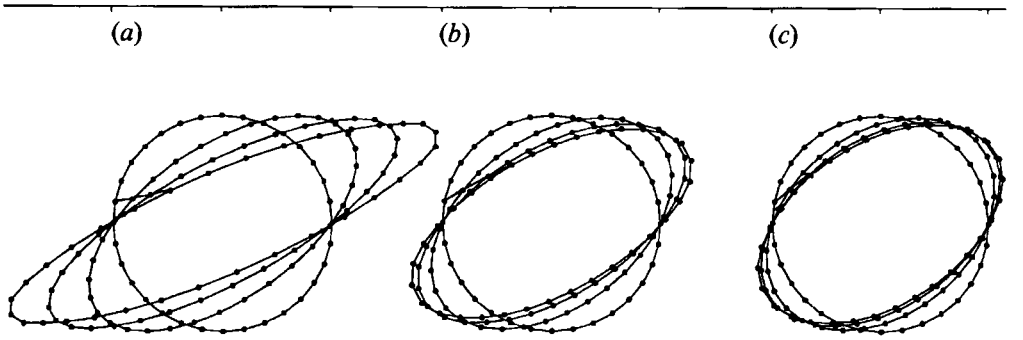

FIGURE 7. Trajectories of marker points in the (x, y)-plane for (*a*) $G = 1.0$, at $kt = 0, 0.735, 1.35, 1.95$; (*b*) $G = 0.1$, at $kt = 0, 0.60, 1.23, 1.80$; (*c*) $G = 0.02$, at $kt = 0, 0.50, 1.00, 1.50$.

numerical results are in good agreement with the predictions of the first-order theory represented by the straight line. The second-order theory of Barthès-Biesel (1980) for membranes that obey the Mooney–Rivlin constitutive equation predicts that the asymptotic deformation curve is convex, that is the slope $\mathrm{d}D^{\infty}_{xy}/\mathrm{d}G$ increases as G is raised to higher values, which contrasts with the behaviour shown in figure 6. This discrepancy might be attributed to the fact that the range of deformation in which the second-order correction makes a dominant contribution over higher-order corrections is limited.

The nature of the interfacial deformation and asymptotic motion at long times may be illustrated by studying the trajectories of the grid points in the (x, y)-plane. In figure 7(*a–c*) we have superposed evolving capsule profiles in the (x, y)-plane for $G = 1, 0.10,$

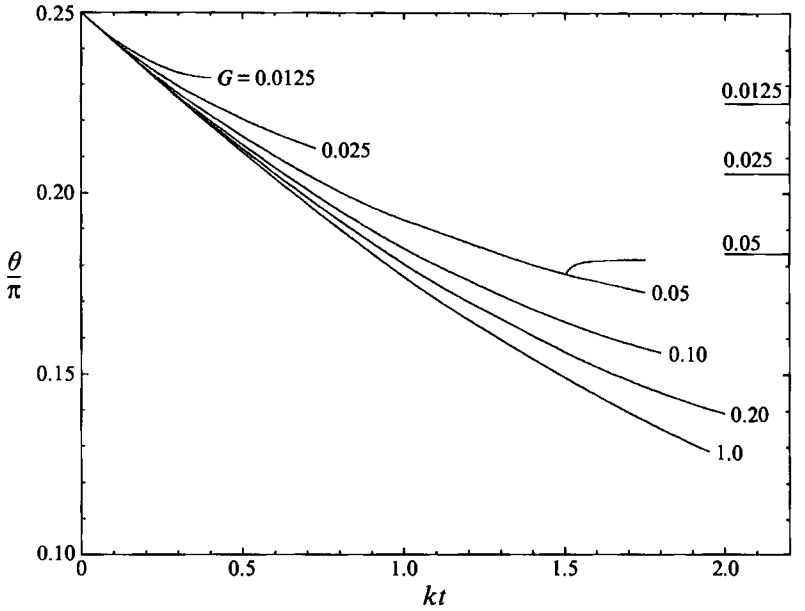

FIGURE 8. The evolution of the inclination angle θ of the major axis of the capsule for a sequence of dimensionless shear rates G. The straight horizontal lines represent the predictions of the second-order theory of Barthès-Biesel (1980) for $G = 0.05, 0.025, 0.0125$.

0.05 at a sequence of characteristic times, marking the trajectories of selected marker points. Figure 7(*a*) shows that the marker points move predominantly under the influence of the shear flow with the elastic tensions offering only weak resistance, with no evidence that the capsule approaches a steady state. In contrast, the motion of the marker points indicated in figure 7(*b*, *c*) is consistent with the approach towards a steady shape. The contours corresponding to last two time instants in each frame, in particular, suggest that the interface executes a tank-treading motion with the marker point rotating around the interface. The character of the tank-treading motion will be discussed later in this section.

Chang & Olbright (1993) reported experimental observations and measurements of the deformation of capsules with polymerized interfaces in simple shear flow. Assuming that the interfaces exhibit linear viscoelastic behaviour and comparing their measurements with the predictions of the linear analysis of Barthès-Biesel & Sgaier (1985), they obtained values for the effective membrane viscosity and elasticity. Furthermore, by plotting the asymptotic deformation D_{xy}^{∞} as a function of the dimensional shear rate G they obtained a curve with a concave shape which is qualitatively similar to the one shown in figure 6 of the present paper. The linear regime of their deformation curve ends at $G = 0.04$ which is in agreement with the results of the present computations.

Chang & Olbright (1993) observed that when the dimensionless shear rate G exceeds a certain value, the capsules deform to a quasi-steady elongated shape, oscillate, and then stretch until the membrane bursts and the contents of the capsule spill into the suspended fluid. Experimental difficulties did not permit the precise evaluation of critical value of G, but in one reported experiment, continued elongation occurred when the deformation parameter D exceeded the value of 0.50 with corresponding dimensionless shear rate as high as $G = 0.066$. Our computations suggest that the critical value of G is close to and somewhat above the value of 0.2. The disagreement

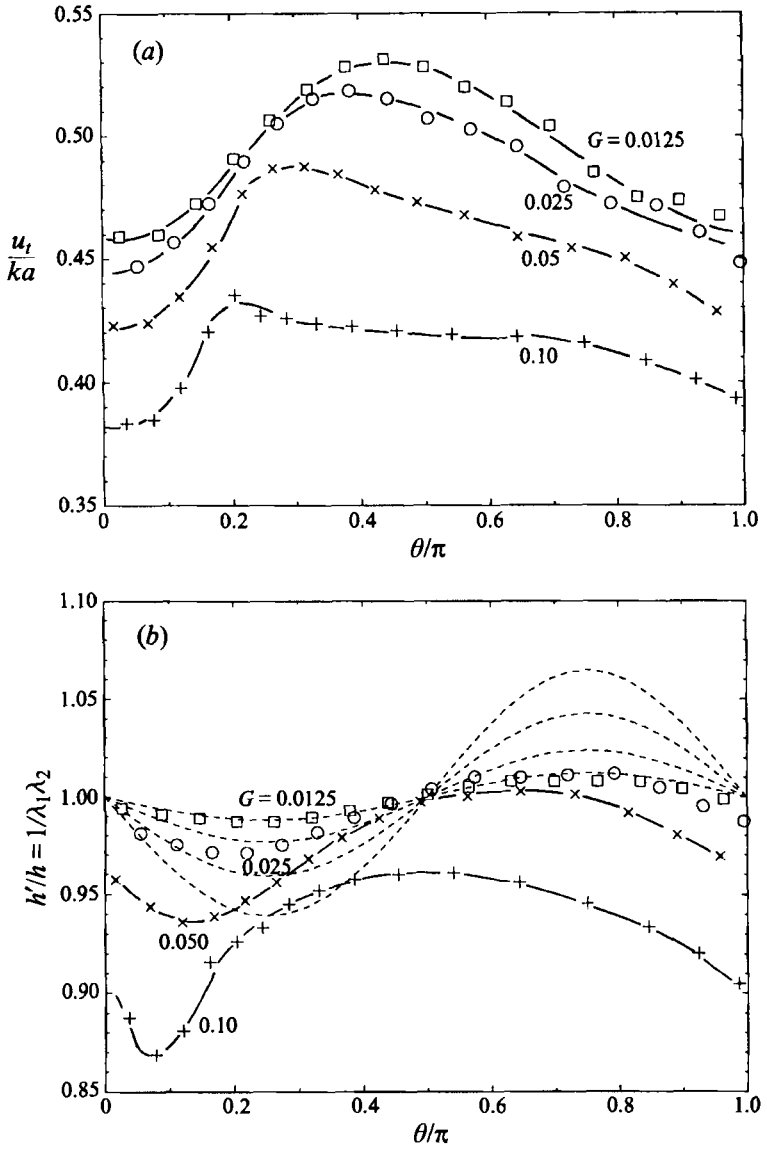

FIGURE 9(*a*,*b*). For caption see facing page.

between computations and observation may be attributed to the facts that (*a*) the unstressed state of the capsules studied by Chang & Olbright was not precisely spherical, (*b*) the viscosity ratio was not exactly equal to one but had a lower value, (*c*) the membrane appeared to have an appreciable surface viscosity and to exhibit plastic deformations.

4.4. *Transient and asymptotic inclinations*

To further describe the nature of the evolving and asymptotic capsule shapes, in figure 8 we plot the inclination angle θ of the major axis of the drop for the cases shown in figure 4. For all values of G with the exception $G = 1$, the results indicate that θ tends to an asymptotic value, with higher deformations corresponding to lower inclinations. Equation (4.1) predicts that the capsule deforms along the principal direction of the

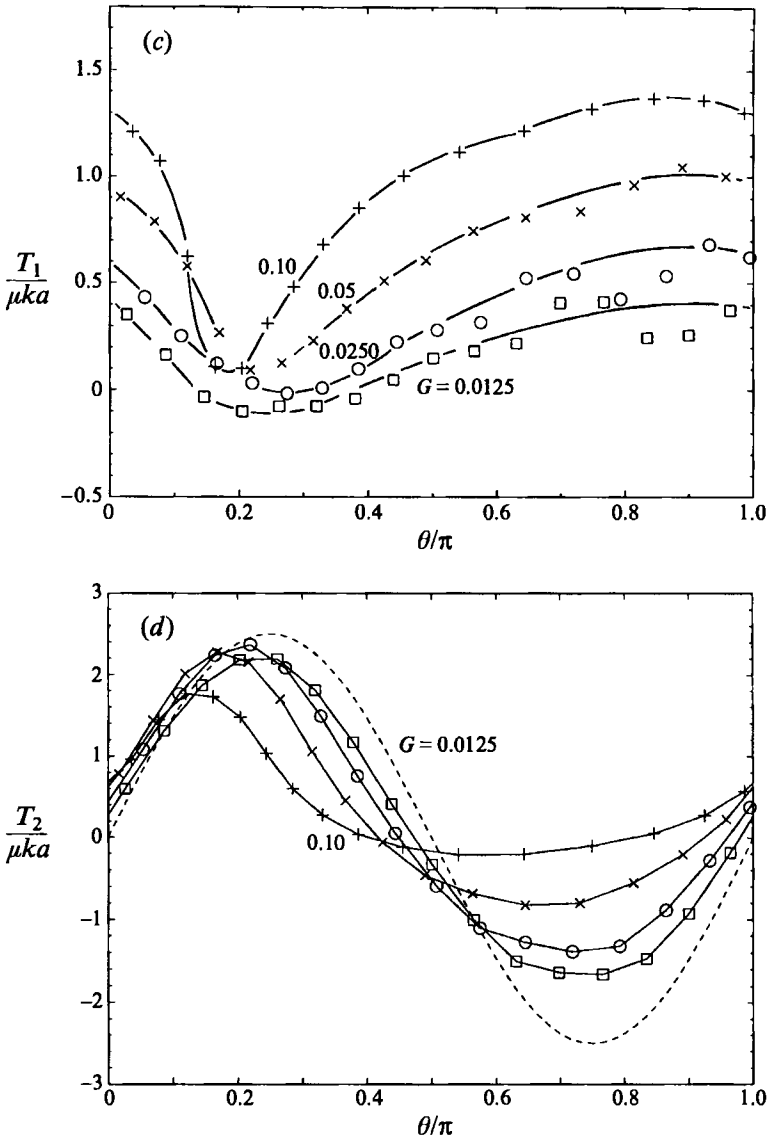

FIGURE 9. Distributions of (*a*) the tangential component of the velocity, (*b*) relative thickness of the membrane $h'/h = 1/\lambda_1\lambda_2$ (the dashed lines show the predictions of the linear model), (*c*) first principal tension T_1 in the (x, y)-plane, (*d*) second principal tension T_2 along the z-axis, around the contour of the capsule in the (x, y)-plane (the dashed line shows the limit for an undeformed spherical capsule); □, $G = 0.0125$, $kt = 0.308$; ○, $G = 0.025$, $kt = 0.593$; ×, $G = 0.05$, $kt = 1.0$; +, $G = 0.10$, $kt = 1.5$.

rate of strain of the shear flow at a 45° angle with respect to the x-axis, but the second-order analysis of Barthès-Biesel (1980) shows that nonlinear effects cause the capsule to incline towards the x-axis. The three horizontal lines in figure 8 represent the predictions of the second-order theory for $G = 0.05, 0.025, 0.0125$ read off figure 7 of Barthès-Biesel (1980). Although computations at long times were prohibited by numerical instabilities, the asymptotic inclinations deduced by extrapolating the numerical results are in qualitative agreement with those predicted by the second-order expansion. The difference between the numerical and asymptotic results is substantial

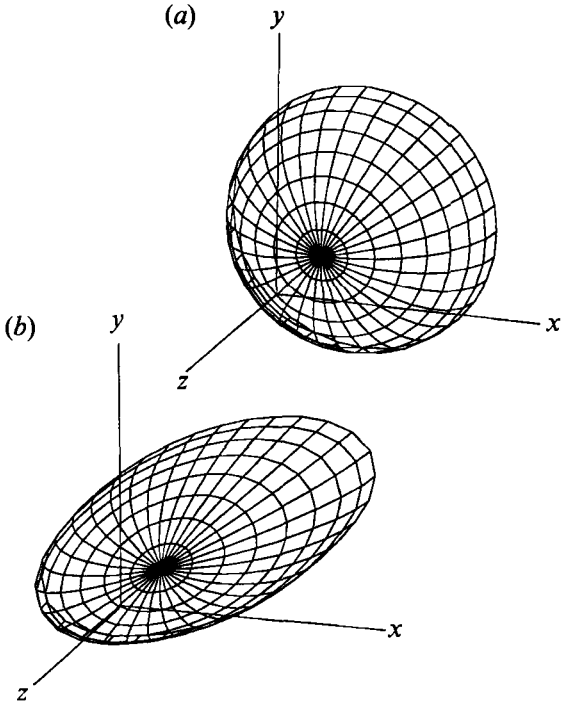

FIGURE 10. The shape of the interfacial $N = 16, M = 8$ grid for $G = 0.10$ at (*a*) $kt = 0$, (*b*) $kt = 1.51$. The interfacial elements remain untwisted at all times, but sawtooth-type oscillations develop at later times.

when the deformations are large, but similar discrepancies exist in the analogous case of liquid drops with constant surface tension (Kennedy *et al.* 1994).

4.5. *Kinematics of interfacial motion*

To further examine the nature of the asymptotic motion at steady state, in figure 9(*a*) we plot the distribution of the tangential component of the velocity around the contour of the capsule at the (x, y)-plane, u_t, as a function of the meridional angle θ for $G = 0.10, 0.05, 0.025, 0.0125$. The associated times fall into the advanced stages of the motion before numerical instabilities have started to become noticeable. The results show that the distribution of the reduced tangential velocity fluctuates around a mean value which increases from about $0.4ka$ when $G = 0.10$, in which case the capsule is substantially deformed, to about $0.5ka$ when $G = 0.0125$, in which case the capsule is only mildly deformed. The value of $0.5ka$ corresponds to the tank-treading velocity of a rigid spherical particle freely rotating in a simple shear flow. The maximum deviation of the tangential velocity from its mean value is about 20%, which indicates that the interface is subjected to a substantial degree of stretching.

The reduced period of rotation of a material point on the membrane in the (x, y)-plane as computed from the distribution of the tangential velocity at long times is $T' = kT/(4\pi) = 1.0, 1.0, 1.1, 1.3$ for $G = 0.10, 0.05, 0.025, 0.0125$. The reference value $T' = 1$ corresponds to a rigid spherical particle rotating freely in a simple shear flow. The fact that T' is larger than 1 is attributed to the increased perimeter of the capsule in the (x, y)-plane due to the capsule's deformation, as well as to the fact that the internal flow deviates from rigid-body rotation. To further illustrate the behaviour of interfacial elements during the deformation, in figure 10(*a*, *b*) we present three-dimensional plots

of the surface co-ordinate over half of the capsule for $G = 0.1$, at the initial instant and at an advanced stage of the evolution at time $kt = 1.51$. The fact that the surface coordinate lines remain smooth and untwisted indicates that point particles on the membrane rotate around the centre of the capsule with comparable tank-treading frequencies.

4.6. *Interfacial stretching, tensions, and rupture*

Rupture of the membrane may be caused by two distinct but somewhat related mechanisms including excessive thinning and excessive tension. Thinning is relevant when the interface is a thin sheet of a three-dimensional elastic material such as rubber or an elastomer. Excessive tension is relevant when the interface consists of a biological membrane with a lipid bi-layer structure such as the membrane of a red blood cell. For instance, measurements have shown that the membrane of the red blood cells fails and the cell hemolyzes when the tension exceeds a threshold that is estimated to be between 5 and 10 dyn cm^{-1} (see, for instance, Lacelle, Evans & Hochmuth 1977).

Rupture due to thinning is discussed by Li *et al.* (1988) and Chang & Olbricht (1993) on the basis of the linear model of Barthès-Biesel & Rallison (1981). Although in the mathematical formulation the membrane thickness h is assumed to remain constant so that the dimensionless shear rate G is independent of time, one requires that the mass of the three-dimensional membrane is conserved and finds that the instantaneous membrane thickness is given by $h'/h = 1/\lambda_1\lambda_2$ where $\lambda_1\lambda_2$ is the interfacial areal stretch. The fact that G is assumed to be uniform and constant in the computations implies that the computed final thickness h' is a mere estimate and probably an upper bound of the actual value. If the area of the interface were locally and thus globally conserved, $\lambda_1\lambda_2 = 1$ at all times, in which case deformation from the spherical shape is not possible.

Examining the distribution of $h'/h = 1/\lambda_1\lambda_2$ over the interface we find that it reaches a minimum in the (x, y)-plane. In figure 9(*b*) we plot $1/\lambda_1\lambda_2$ around half the capsule contour in the (x, y)-plane as a function of the meridional angle θ. The dashed lines show the predictions of the linear model represented by $\ln(\lambda_1\lambda_2) = 2x'y'(2J-3K)/a^2$ where the position vector $\boldsymbol{x}'$ and dimensionless functions J and K are defined in (4.2) and (4.3) (Barthès-Biesel & Rallison 1981, p. 263). The numerical results for $G = 0.0125$ and 0.0250 yield nearly sinusoidal distributions that are in good agreement with the predictions of the linear model. At these low deformations, the ratio h'/h is close to 1, with values lower than 1 in the first quadrant indicating that the membrane has been stretched, and higher than 1 in the second quadrant indicating that the membrane has been compressed. At higher values of G the ratio h'/h is less than 1 over the entire contour of the capsule with a minimum near the major axis of the capsule. This behaviour suggests that when thinning is responsible for rupture, the membrane will fail at a point that is close to the axis of maximum deformation, which is in qualitative agreement with the observations of Chang & Olbright (1993).

To investigate the alternative mechanism of membrane failure due to excessive tension, we consider the distribution of the two principal tensions over the trace of the membrane in the (x, y)-plane. The first principal tension T_1 acts tangentially to the contour of the membrane in the (x, y)-plane, and the second principal tension T_2 acts in a direction that is perpendicular to the (x, y)-plane, that is, it points in the azimuthal direction along the z-axis. In figure 9(*c*, *d*) we plot the distributions of T_1 and T_2 around half the capsule contour as a function of the meridional angle θ for several values of G. The oscillations observed in figure 9(*c*) at low values of G are probably due to the fact that the numerical error becomes comparable to the actual magnitude of the computed physical variable. The dashed line in figure 9(*d*) represents the limit

for an undeformed spherical capsule, corresponding to $G = 0$, described by $T_2/\mu ka = 2.5 \sin 2\theta$; since the trace of the capsule in the (x, y)-plane does not deform, the corresponding first principal tension is equal to zero (Barthès-Biesel 1980). The numerical results are in agreement with the analytical predictions at small deformations.

Two important features emerging from figure 9(*c*, *d*) are that, as the dimensional shear rate G is raised, the magnitude of T_1 increases whereas the magnitude of T_2 decreases, and the distributions of T_1 and T_2 are out of phase with each other. At small deformations the distributions are smooth, but at larger deformations they exhibit sharp variations around the points of extrema. Furthermore, at small deformations the tensions can be either tensile or compressive, whereas at large deformation they are tensile over the entire contour of the capsule. The magnitude of T_2 is significantly higher than that of T_1 at small and moderate deformations, but at larger deformations the two tensions assume comparable values with T_2 prevailing over T_1. In all cases T_2 obtains a maximum value close to the axis of maximum deformation, which will be the point of rupture when the elastic tensions may no longer be supported by the membrane. Since maximum thinning also occurs at that point, the point where the membrane is expected to fail will be insensitive to the precise mechanism of rupture.

To this end, we must emphasize that the physical relevance of the above conclusions is undermined by the use of a simplified interfacial constitutive equation which is certain to fail at the critical conditions for rupture. Furthermore, the presence of tank-treading motion implies that a certain piece of membrane material is subjected to high tensions only for a limited amount of time, and the frequency of cyclic loading may be a relevant parameter as far as determining membrane failure.

4.7. *Rheology of dilute suspensions*

We turn next to consider the rheological properties of a dilute suspension of capsules in simple shear flow. In figure 11(*a–c*) we plot the evolution of the shearing component of the particle stress tensor Σ_{xy} and first and second normal stress differences $N_1 = \Sigma_{xx} - \Sigma_{yy}$, $N_2 = \Sigma_{yy} - \Sigma_{zz}$, all reduced with respect to the corresponding shearing component for a suspension of rigid spherical particles which is denoted by Σ^S_{xy}. The dashed lines in figure 11(*a*) represent the results of the linear theory of Barthès-Biesel & Rallison (1981) which shows that

$$\Sigma_{xy}/\Sigma^S_{xy} = -\tfrac{7}{10}(\tfrac{1}{2}L + \tfrac{1}{5}M), \tag{4.5}$$

where the dimensionless functions L and M are given in (4.4). The agreement between the asymptotic predictions and the numerical computations is excellent at small deformations but becomes worse at moderate and large deformations. The asymptotic theory predicts that the ratio $\Sigma_{xy}/\Sigma^S_{xy}$ tends to 1 at large times irrespective of the value of G, whereas the numerical results show that $\Sigma_{xy}/\Sigma^S_{xy}$ tends to asymptotic values that become smaller as G is raised. This suggests that a dilute suspension of capsules in simple shear flow behaves like a shear-thinning medium, in agreement with the results of the second-order theory of Barthès-Biesel & Chhim (1981). When the surface elasticity is large or G is small, the membrane rotates like a rigid shell, the flow within the capsule represents rigid body rotation, and the ratio $\Sigma_{xy}/\Sigma^S_{xy}$ becomes equal to 1.

Figure 11(*b*) shows that, as G is increased, the asymptotic value of the first normal stress difference N_1 increases because the capsule attains an increasingly non-spherical shape and therefore promotes the spatial anisotropy in the suspension. The estimated asymptotic values of N_1 for $G = 0.05, 0.025, 0.0125$ are in fair agreement with those predicted by the second-order theory of Barthès-Biesel & Chhim (1981), which yields

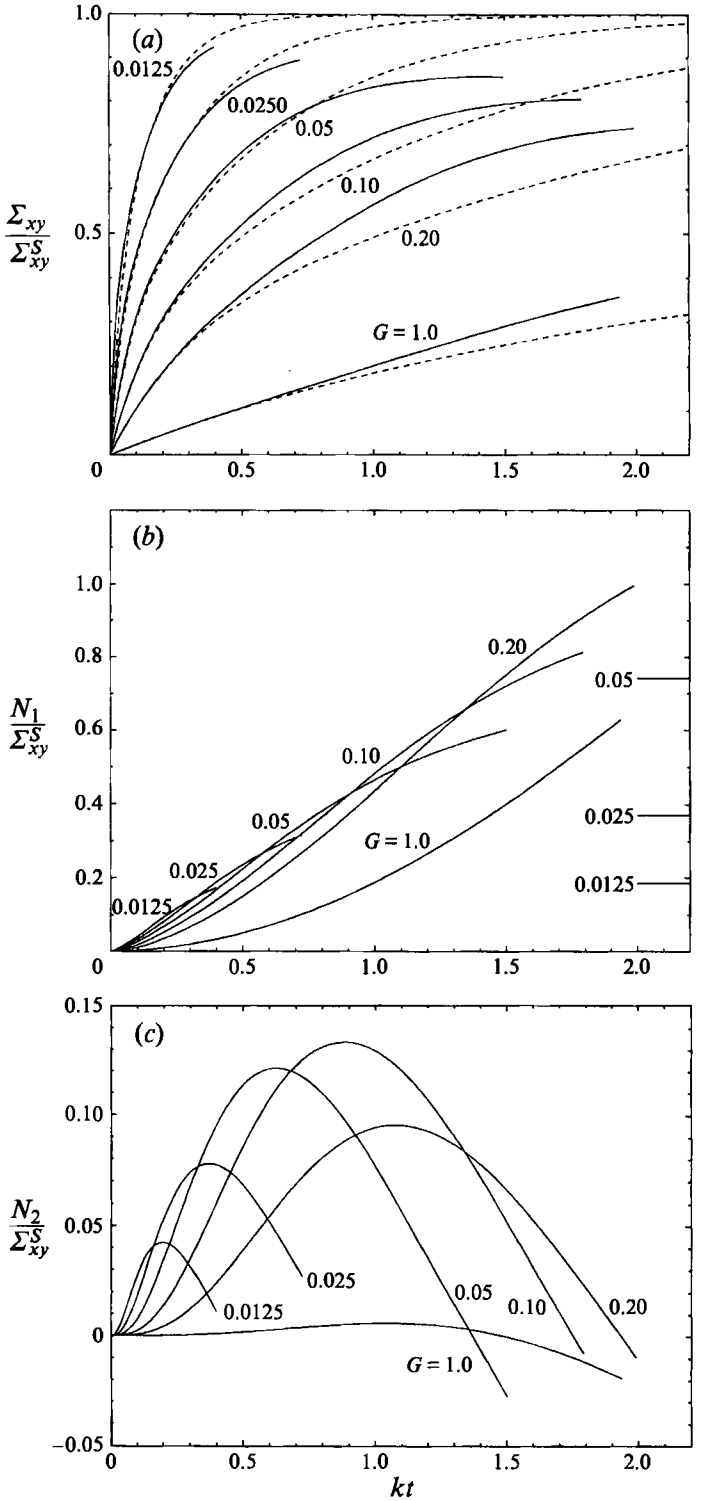

FIGURE 11. The evolution of (*a*) the shear component of the particle stress tensor and (*b*, *c*) first and second normal stresses for a dilute suspension of capsules, at a sequence of dimensionless shear rates G, reduced with respect to the shear component Σ^S_{xy} for a dilute suspension of rigid spheres. Dashed lines in (*a*) show the linear theory of Barthès-Biesel & Rallison (1981).

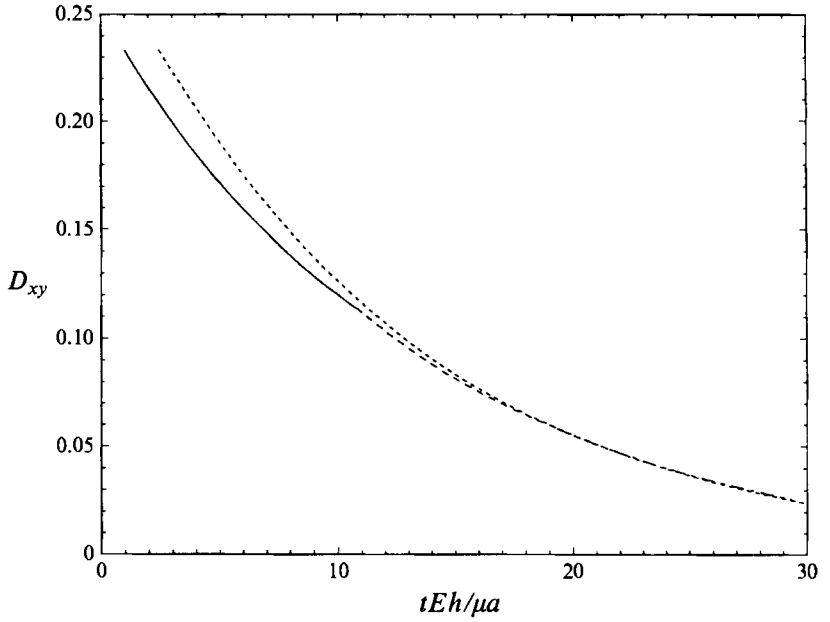

FIGURE 12. Evolution of the deformation parameter D_{xy} during relaxation where the shear flow is stopped and the capsule is allowed to relax back to the spherical shape, for three different initially deformed capsule shapes. The short dashed line shows the predictions of the first-order linear theory.

$N_1/\Sigma^S_{xy} = 14.86G$. Figure 11(*c*) shows that N_2 tends to attain negative values at long times, which suggests that a dilute suspension behaves like a non-Newtonian fluid with some elastic properties similar to those exhibited by polymeric solutions.

4.8. *Relaxation to the spherical shape*

We performed a series of computations in which the incident shear flow was stopped at a certain time during the evolution, and the capsule was allowed to relax back to the spherical shape. The numerical method worked well for an extended period of time during the initial relaxation period, but numerical instabilities eventually set in bringing the computations to an end. In figure 12 we plot the deformation D_{xy} as a function of the dimensionless time $tEh/\mu a$ during relaxation. The three curves shown with the solid, dashed, and dot-dashed lines correspond to three different initial capsule shapes taken from the evolution of spherical capsules with $G = 0.05$, 0.025, and 0.0125. The origin of time in the three computations has been shifted to match corresponding values of D_{xy}. The orientation of the capsules remained virtually constant during the relaxation.

The three curves in figure 12 form a natural continuation of each other, and this indicates that, for a given value of D_{xy}, the relaxation of the capsule depends weakly on the initial shape. The short-dashed line in figure 12 represents the predictions of the first-order model of Barthès-Biesel. The analytical predictions are in good agreement with the numerical results at small deformations. Replotting the data on a linear–log scale we obtain a straight line with a well-defined slope. The negative of the inverse of the slope defines the relaxation time $\tau = 12.7\mu a/Eh$ which may be used to assess the value of Eh from measurements of the capsule deformation during relaxation. The small-deformation theories of Brunn (1980*a*, *b*) and Barthès-Biesel & Rallison (1981, p. 263) reveal the presence of two relaxation times, $\tau = 12.1\mu a/Eh$ and $1.36\mu a/Eh$, the

first of which is relevant in the late stages of the motion. The small difference between the computed and the theoretical relaxation time may be attributed to numerical error or to the effect of the shorter scale.

5. Ellipsoidal capsules

In the second part of the numerical investigation we consider capsules with oblate ellipsoidal unstressed shapes resembling resting normal red blood cells. The motion of the capsules is a function of the dimensionless shear rate $G = \mu ka/Eh$ defined with respect to the equivalent capsule radius $a = (3V/4\pi)^{1/3}$ where V is the capsule volume, initial aspect ratio b/c of the generating ellipse, and initial angle θ_0 between the major axis of the trace of the capsule in the (x, y)-plane and the x-axis.

In figure 13(*a*) we plot the evolution of the deformation parameter D_{xy} for capsules with $b/c = 2.0$ and $\theta_0 = \pi/4$, for a series of dimensionless shear rates; at the initial instant $D_{xy} = 1/3$. The general features of the deformation curves are similar to those for the spherical capsules discussed in the preceding section. The results suggest that, at long times, the capsules reach asymptotic shapes for all values of G, except for the highest shear rate $G = 1$, with higher values of G corresponding to higher asymptotic deformations. When $G = 1$ the deformation curve indicates continued elongation, possibly leading to membrane rupture. The critical value of G above which the capsules fail to assume stationary shapes is estimated to be close to but below the value of 0.20, which is comparable to the corresponding critical value for spherical capsules.

The behaviour of the inclination angle is illustrated in figure 13(*b*). We observe that all curves fall on top of each other, which is a significant departure from the behaviour of spherical capsules. The rate of rotation is significant even when the deformation D_{xy} appears to have reached its asymptotic value. Unfortunately, the computations had to be terminated at the point where numerical instabilities placed a pragmatic limit on the size of the time step. Further computations discussed below for different inclinations θ_0 will indicate that, at long times, θ tends to an asymptotic value that is close to 0.13π. The capsule rotates because, during the initial stages of the motion, the particle behaves like rigid body immersed in a simple shear flow, and the effect of deformation is masked by the global rotation.

To illustrate the nature of the transient deformation, in figure 14(*a*, *b*) we present successive profiles of the contour of the capsule in the (x, y)-plane for $G = 0.025$ and 0.10, indicating the position of the marker points. At the latest time depicted in figure 14(*a*), the upper and lower main body of the capsule has reached a nearly steady state with the marker points tank-treading around the contour, but the tip of the capsule still undergoes substantial deformation. At the latest time depicted in figure 14(*b*) the entire body of the capsule appears to have reached a quasi-steady state, but figure 13(*b*) indicates that the capsule continues to rotate like a rigid body with small changes in shape.

We turn next to illustrate the effect of initial inclination angle θ_0 by discussing differences in the behaviour of a capsule for $G = 0.10$. In figure 15(*a*, *b*) we plot the evolution of D_{xy} and θ for $\theta_0 = 0, 0.13\pi, 0.25\pi, 0.35\pi$, and in figure 15(*c*) we present successive profiles of the contour of the capsule in the (x, y)-plane for $\theta_0 = 0.13\pi$ and 0. The value 0.13π was selected because it is close to the asymptotic inclination angle of a deformed spherical capsule with $D_{xy} = 1/3$ discussed in §3. Figure 15(*a*) shows that the time it takes for the capsule to deform and attain the asymptotic shape is a strong function of θ_0, with the fastest rate of deformation at the initial instant occurring for $\theta_0 = 0.25\pi$. In this case, the major axis of the capsule is aligned with the first

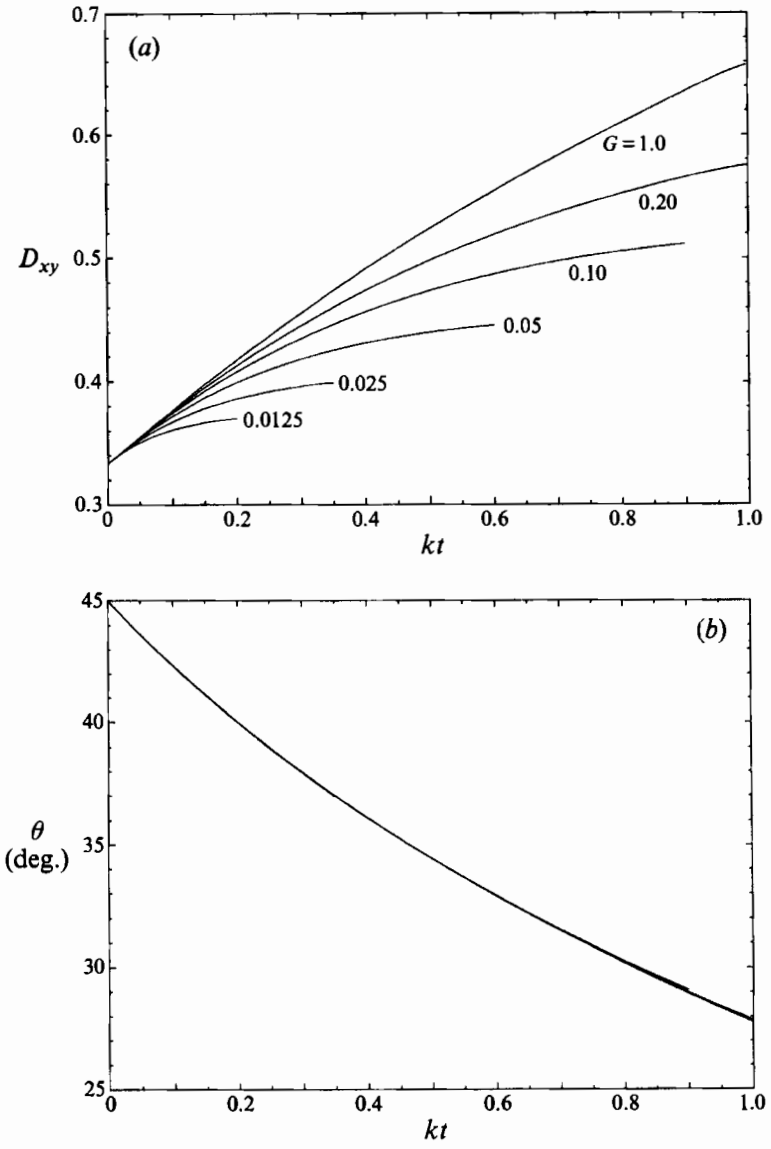

FIGURE 13. Evolution of (*a*) the deformation parameter D_{xy}, and (*b*) inclination angle θ for an oblate spheroidal capsule resembling a disk, with aspect ratio $b/c = 2.0$, initial orientation $\theta_0 = \pi/4$, and several values of the dimensionless shear rate.

principal direction of the incident flow and is therefore subjected to stronger deforming action. The computations with $\theta_0 = 0$ and 0.13π became unstable at a relatively early stage of the deformation; in the second case, the surface grid suffers severe distortions because the capsule must rotate in the counterclockwise direction towards the steady inclination angle. Figure 15(*b*) suggests that the asymptotic inclination angle at long times is common in all three and close to 21°.

We examine next the kinematical behaviour of the membrane and development of tensions with an objective of identifying the effect of the aspect ratio of the unstressed shape. In figure 16(*a*, *b*) we plot the distributions of the tangential component of the velocity along the trace of the contour of the capsule in the (x, y)-plane, the

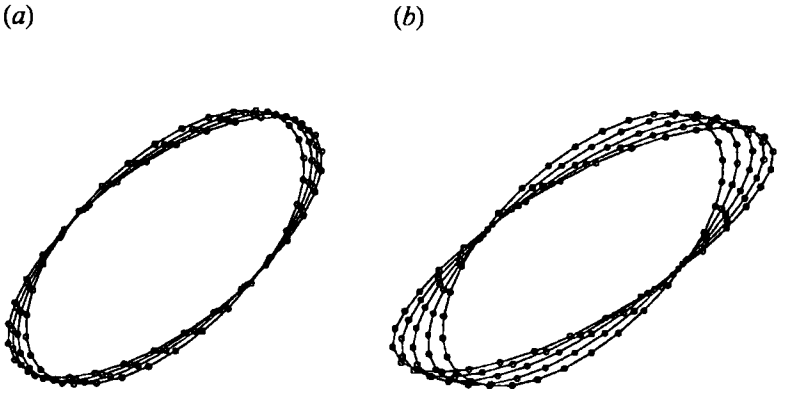

FIGURE 14. Trajectories of marker points in the (x, y)-plane for (*a*) $G = 0.025$, at $kt = 0, 0.10, 0.20, 0.30$; (*b*) $G = 0.1$, at $kt = 0.195, 0.395, 0.595, 0.795$.

instantaneous membrane thickness $h'/h = 1/\lambda_1 \lambda_2$, and the principal tensions T_1 and T_2, against the meridional angle θ around the contour of the capsule in the (x, y)-plane. The two-figures correspond to $G = 0.10$ and $kt = 0.595$ with initial orientations $\theta_0 = 0.25\pi$ and 0.13π, the corresponding contour shapes are depicted in figure 15(*c*). The qualitative features of corresponding distributions in figure 16(*a*, *b*) are similar, although significant quantitative differences are apparent. In both cases the instantaneous tank-treading velocity shows substantial variation along the capsule indicating that the membrane is subject to a significant rate of compression and stretching. Although spheroidal capsules with purely elastic interfaces are only approximate models of red blood cells, it is nevertheless interesting to compare the computed tank-treading frequency f of point particles in the (x, y)-plane with that measured in the laboratory for red blood cells, which is around $f = 0.22k$. The present results for $a/b = 2$ show that $f = 0.30k$, which is in the same range with the experimentally measured values.

The distributions of h'/h reveal that minimum membrane thickness occurs at a point over the main body of the cell located a significant distance away from the major axis of the capsule. This behaviour is different from that of the spherical capsules discussed in §3 where maximum thinning occurred near the tip. The distribution of the principal tensions are also different from those for the spherical capsules illustrated in figure 9(*c*, *d*). In the case of the ellipsoidal particle, the first principal tension T_1 is consistently higher than the second principal tension, and the point at which T_1 is maximum is near the middle of the main body of the cell and close to the point of maximum thinning. These results indicate that the location of maximum thinning and possible membrane rupture is sensitive to the unstressed particle shape.

Zhou & Pozrikidis (1995) studied the deformation of capsules with oblate spheroidal unstressed shapes bounded by incompressible membranes and computed the developing membrane tensions. Their computations showed that the point of maximum tension is located over the upper body of the capsule close to the rear end. Comparing their results with the present observations indicates that the mechanical properties of the membrane play an important role in determining the location of rupture.

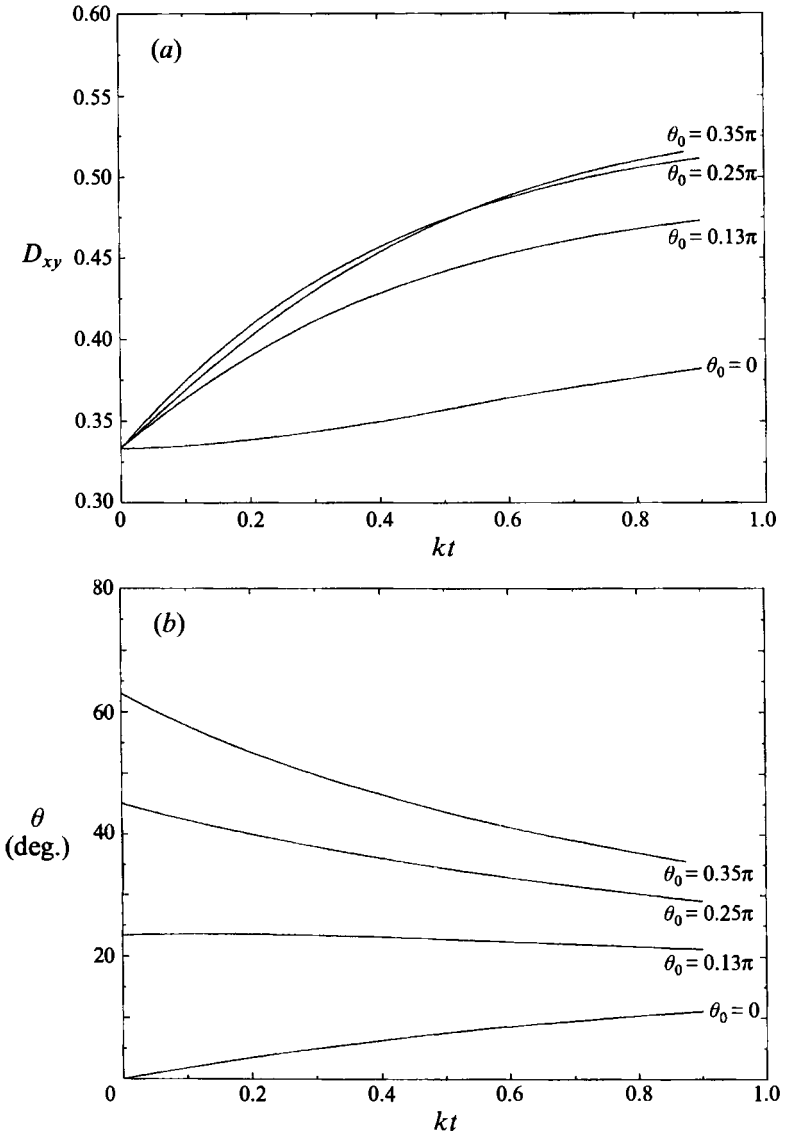

FIGURE 15(*a*,*b*). For caption see facing page.

We performed a series of computations in which the incident shear flow was stopped and the deformed capsule was allowed to relax back to the initial shape. In figure 17 we plot the excess deformation $D_{xy} - D^0_{xy}$ where $D^0_{xy} = 1/3$ corresponds to the unstressed shape, as a function of the dimensionless time $tEh/\mu a$ on a linear–log scale during relaxation, and obtain a nearly straight line. The two curves shown with the solid and dashed line correspond to two different initial capsule shapes taken from the deformation of a capsule with $G = 0.10$; the origin of time was shifted to match corresponding values of D_{xy}. The negative of the inverse of the slope of the straight line defines the relaxation time $\tau = 7.0\mu a/Eh$ which is substantially smaller than the value 12.7 obtained previously for the spherical capsules. Thus, the higher the aspect ratio of the undeformed shape, the faster the capsules relax back to the unstressed state.

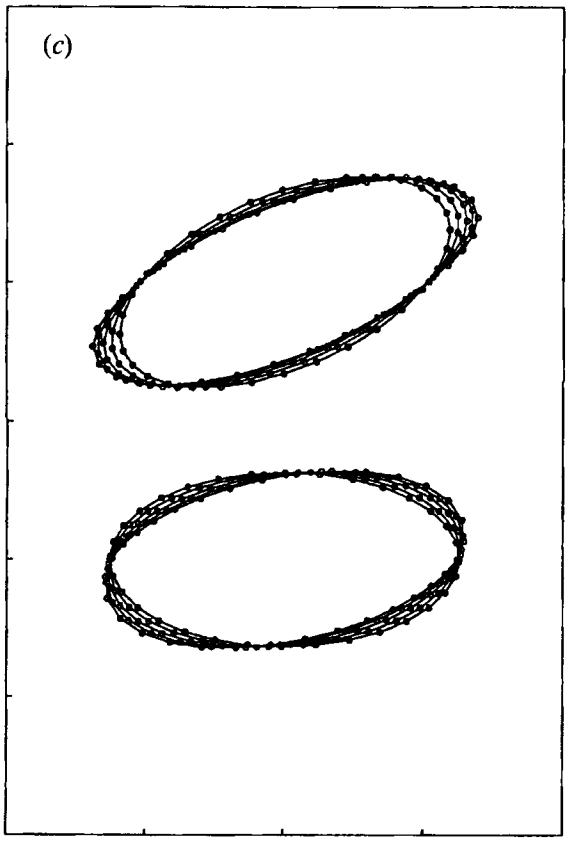

FIGURE 15. Evolution of (*a*) the deformation parameter D_{xy}, and (*b*) inclination angle θ for an oblate spheroidal capsule with aspect ratio $b/c = 2.0$ at $G = 0.10$, corresponding to different initial inclination angles θ_0. (*c*) Trajectories of marker points in the (x, y)-plane for $\theta_0 = 0.13\pi$ (top) and $\theta_0 = 0$ (bottom), at times $kt = 0, 0.195, 0.395, 0.595, 0.795$.

Schmid-Schönbein (1975) reported that the relaxation time of red blood cells in a dextran solution with $\mu = 60$ cP is 0.6 s. Taking $a = 3$ mm, $Eh = 0.0025$ dyn cm^{-1} yields $\tau = 0.5$ s which is in the same range as the observed value.

Computations with capsules of higher aspect ratio a/b were hindered by high computational cost. A capsule with $a/b = 3$ has $D^0_{xy} = 0.5$ in the unstressed state, which is close to the point where the 16 by 8 grid becomes unable to describe the shape of the membrane with sufficient resolution. Furthermore, computations using the strain-energy function for the red blood cell membrane given in (2.14) with the values of B and C proposed by Skalak *et al.* (1973) were hindered by numerical instabilities attributed to the fact that the elastic tensions are strong functions of the areal stretch.

6. Summary and comments

We have developed a boundary element method suitable for computing the finite deformation of capsules enclosed by elastic membranes whose mechanical behaviour is expressed by a general strain-energy function. In its present implementation, the method is capable of describing the deformation of spherical and spheroidal capsules with low and moderate aspect ratio whose interface exhibits a simple type of elastic

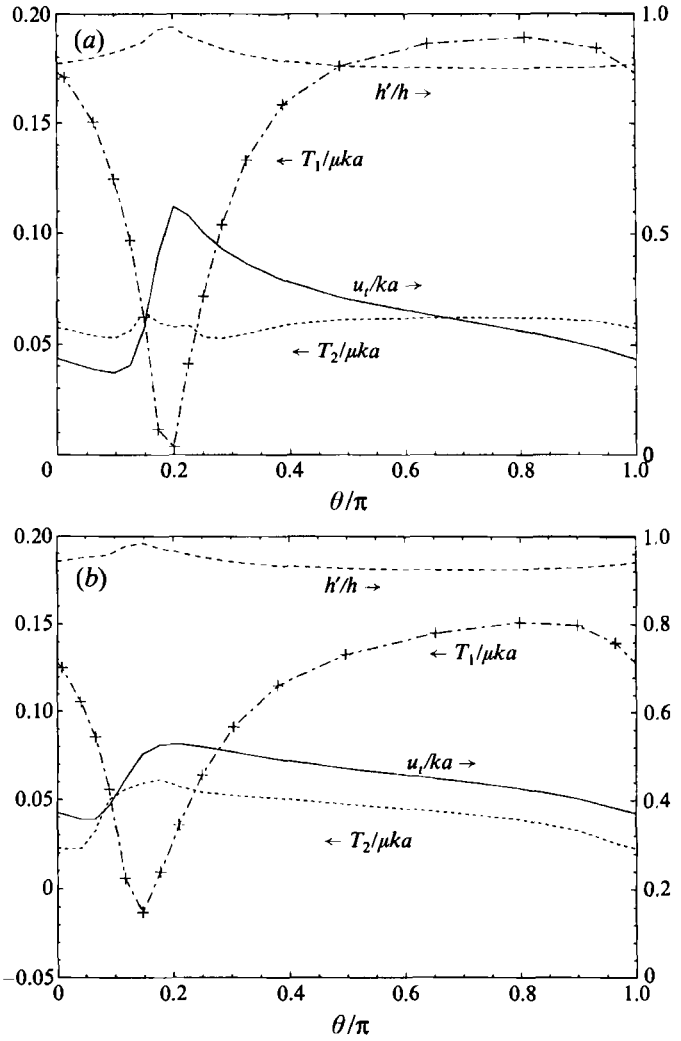

FIGURE 16. Distributions of the tangential component of the velocity along the trace of the contour of the capsule in the (x, y)-plane, reduced membrane thickness $h'/h = 1/(\lambda_1 \lambda_2)$, and the principal tensions T_1 and T_2, for $G = 0.10$ and $kt = 0.595$, corresponding to two initial inclinations (*a*) $\theta_0 = 0.25\pi$ and (*b*) $\theta_0 = 0.13\pi$.

behaviour. For highly nonlinear elastic behaviour and capsules with highly eccentric shapes, the effectiveness of the method is limited by numerical instabilities due to the grid distortion.

For small deformations, the numerical results for spherical capsules are in agreement with the predictions of the first-order small-deformation theory of Barthès-Biesel and coworkers in all aspects of the motion. For moderate and large deformations there are significant differences in both the transient and asymptotic capsule shapes, and the distribution of the elastic tensions. Such differences, however, are familiar from the analogous case of liquid drops. The point of maximum membrane thinning is found to be close to the point where one of the principal tensions assumes its maximum value, and this indicates that the point where the membrane is likely to rupture is insensitive to the precise mechanism of rupture. The aspect ratio of capsules with non-spherical

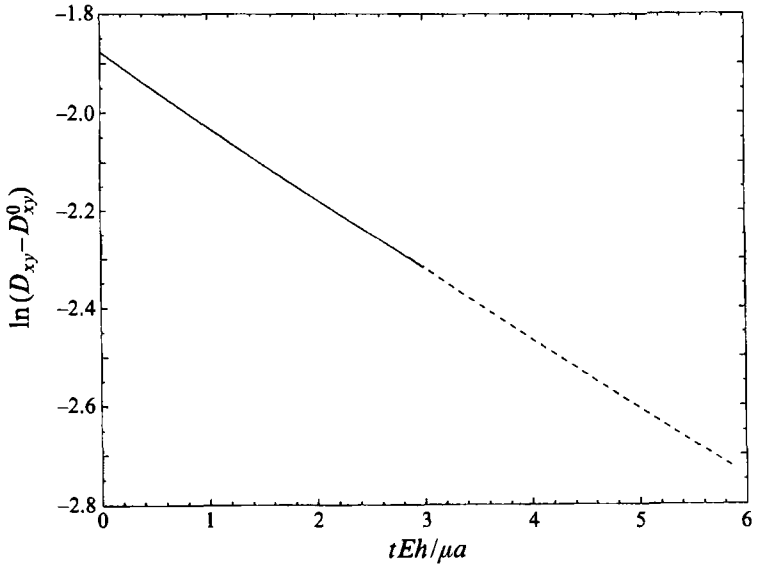

FIGURE 17. Evolution of the deformation parameter D_{xy} during relaxation to the spheroidal shape. The solid and dashed lines correspond to two different initial capsule shapes.

unstressed shapes has a significant effect on the kinematical behaviour of the membrane and the development of tensions. Comparisons between the numerical results and the recent laboratory observations of Chang & Olbricht (1993) showed qualitative similarities but also quantitative discrepancies. The latter are attributed to a number of factors including the effect of surface viscosity.

Capsules enclosed by purely elastic membranes are only approximate models of red blood cells, and this is evidenced by the fact that the purely elastic membranes undergo significant stretching and may not be considered to be incompressible. In the present computations, the area of small interfacial patches may increase by as much as 10% of the initial value. Nevertheless, the results for the tank-treading frequency of oblate spheroidal capsules with aspect ratio $b/c = 2$, and for the relaxation time to the unstressed shape, are found to be in the same range as those measured in the laboratory for normal red blood cells. Incorporating an isotropic surface tension with an objective of satisfying the condition of membrane incompressibility, and accounting for the effect of surface viscosity, will improve the model, but is currently prohibited by increased computational cost.

This research is supported by the National Science Foundation, Grant CTS-9216176, and the Department of Energy, Grant DE-FG03-94ER25192. Additional support was provided by the Exxon Education Foundation.

REFERENCES

BARTHÈS-BIESEL, D. 1980 Motion of a spherical microcapsule freely suspended in a linear shear flow. *J. Fluid Mech.* **100**, 831–853.

BARTHÈS-BIESEL, D. 1991 Role of interfacial properties on the motion and deformation of capsules in shear flow. *Physica* A **172**, 103–124.

BARTHÈS-BIESEL, D. & CHHIM, V. 1981 The constitutive equation of a dilute suspension of spherical microcapsules. *Intl J. Multiphase Flow* **7**, 493–505.

BARTHÈS-BIESEL, D. & RALLISON, J. M. 1981 The time-dependent deformation of a capsule freely suspended in a linear shear flow. *J. Fluid Mech.* **113**, 251–267.

BARTHÈS-BIESEL, D. & SGAIER, H. 1985 Role of membrane viscosity in the orientation and deformation of a spherical capsule suspended in shear flow. *J. Fluid Mech.* **160**, 119–135.

BATCHELOR, G. K. 1970 The stress system in a suspension of force-free particles. *J. Fluid Mech.* **41**, 545–570.

BRUNN, P. O. 1980*a* On the rheology of viscous drops surrounded by an elastic shell. *Biorheology* **17**, 419–430.

BRUNN, P. O. 1980*b* The deformation of a viscous particle surrounded by an elastic shell in a general time-dependent linear flow field. *J. Fluid Mech.* **126**, 533–544.

CHANG, K. S. & OLBRIGHT, W. L. 1993 Experimental studies of the deformation of a synthetic capsule in extensional flow. *J. Fluid Mech.* **250**, 587–608.

EVANS, E. A. & SKALAK, R. 1980 *Mechanics and Thermodynamics of Biomembranes.* CRC Press.

KENNEDY, M. R., POZRIKIDIS, C. & SKALAK, R. 1994 Motion and deformation of liquid drops and the rheology of dilute emulsions in simple shear flow. *Computers Fluids* **23**, 251–278.

LACELL, P. L., EVANS, E. A. & HOCHMUTH, R. M. 1977 Erythrocyte membrane elasticity, fragmentation and lysis. *Blood Cells* **3**, 335–350.

LEE, J. S. & FUNG, Y. C. 1969 Modeling experiments of a single red blood cell moving in a capillary blood vessel. *Microvascular Res.* **1**, 221–243.

LI, X. Z., BARTHÈS-BIESEL, D. & HELMY, A. 1988 Large deformations and burst of a capsule freely suspended in an elongational flow. *J. Fluid Mech.* **187**, 179–196.

LONGUET-HIGGINS, M. S. & COKELET, E. D. 1976 The deformation of steep surface waves on water I. A numerical method of computation. *Proc. R. Soc. Lond.* A **350**, 1–26.

NOVOZHILOV, V. V. 1962 *Theory of Elasticity.* Pergamon Press.

PESKIN, C. S. & MCQUEEN, D. M. 1980 Modeling prosthetic heart valves for numerical analysis of blood flow in the heart. *J. Comput. Phys.* **37**, 113–132.

POZRIKIDIS, C. 1992 *Boundary Integral and Singularity Methods for Linearized Viscous Flow.* Cambridge University Press.

POZRIKIDIS, C. 1993 On the transient motion of ordered suspensions of liquid drops. *J. Fluid Mech.* **246**, 301–320.

POZRIKIDIS, C. 1994 Effects of surface viscosity on the deformation of liquid drops and the rheology of dilute emulsions in simple shearing flow. *J. Non-Newtonian Fluid Mech.* **51**, 161–178.

RICHARDSON, E. 1974 Deformation of haemolysis of red blood cells in shear flow. *Proc. R. Soc. Lond.* A **338**, 129–153.

SCHMID-SCHÖNBEIN, H. 1975 Erythrocyte rheology and the optimization of mass transport in the microcirculation. *Blood Cells* **1**, 285–306.

SECOMB, T. W. & SKALAK, R. 1982 Surface flow of viscoelastic membranes in viscous fluids. *Q. J. Mech. Appl. Maths* **35**, 233–247.

SKALAK, R., TÖZEREN, A., ZARDA, R. P. & CHIEN, S. 1973 Strain energy function of red blood cell membranes. *Biophys. J.* **13**, 245–264.

STONE, H. 1994 Dynamics of drop deformation and breakup in viscous fluids. *Ann. Rev. Fluid Mech.* **26**, 65–102.

SUTERA, S. P., SESHADRI, V. P., GROCE, A. & HOCHMUTH, R. M. 1970 Capillary blood flow. II. Deformable model cells in tube flow. *Microvascular Res.* **2**, 420–433.

ZHOU, H. & POZRIKIDIS, C. 1995 Deformation of capsules with incompressible interfaces in simple shear flow. *J. Fluid Mech.* **283**, 175–200.